

Kerr-enhanced optomechanical cooling in the unresolved-sideband regime

N. Diaz-Naufal ¹, L. Deeg ^{2,3}, D. Zöpfl ^{2,3}, C. M. F. Schneider ^{2,3}, M. L. Juan ⁴, G. Kirchmair ^{2,3} and A. Metelmann ^{1,5,6}

¹*Dahlem Center for Complex Quantum Systems and Fachbereich Physik, Freie Universität Berlin, 14195 Berlin, Germany*

²*Institute for Quantum Optics and Quantum Information, Austrian Academy of Sciences, 6020 Innsbruck, Austria*

³*University of Innsbruck, Institute for Experimental Physics, 6020 Innsbruck, Austria*

⁴*Institut Quantique and Département de Physique, Université de Sherbrooke, Sherbrooke, Québec, J1K 2R1, Canada*

⁵*Institute for Quantum Materials and Technology and Institute for Theory of Condensed Matter,*

Karlsruhe Institute of Technology, 76131 Karlsruhe, Germany

⁶*Institut de Science et d'Ingénierie Supramoléculaires, UMR No. 7006, CNRS, University of Strasbourg, 67081 Strasbourg, France*



(Received 25 October 2024; revised 28 March 2025; accepted 7 April 2025; published 5 May 2025)

Dynamical backaction cooling has been demonstrated to be a successful method for achieving the motional quantum ground state of a mechanical oscillator in the resolved-sideband regime, where the mechanical frequency is significantly larger than the cavity decay rate. Nevertheless, as mechanical systems increase in size, their frequencies naturally decrease, thus bringing them into the unresolved-sideband regime, where the effectiveness of the sideband cooling approach decreases. Here we demonstrate, however, that this cooling technique in the unresolved-sideband regime can be significantly enhanced by utilizing a nonlinear cavity as shown in the experimental work of Zöpfl *et al.* [*Phys. Rev. Lett.* **130**, 033601 (2023)]. The above arises due to the increased asymmetry between the cooling and heating processes, thereby improving the cooling efficiency. In addition, we show that injecting a squeezed vacuum into the nonlinear cavity paves the way to ground-state cooling of the mechanical mode. Notably, the required squeezing parameters are far less stringent than in the linear case, simplifying experimental implementation.

DOI: [10.1103/PhysRevA.111.053505](https://doi.org/10.1103/PhysRevA.111.053505)

I. INTRODUCTION

Besides emerging to create highly sensitive detectors for gravitational waves [1,2], the field of optomechanics has undergone enormous progress in recent years [3]. Among the achievements are the detection of displacements below the standard quantum limit [4,5], the preparation of non-classical states of motion [6,7], and the demonstration of strong optomechanical coupling in both the microwave and optical regimes [8,9]. Due to the controllable interaction between light and mechanics, optomechanics is considered a fundamental resource for realizing hybrid quantum devices of otherwise incompatible degrees of freedom for numerous applications in quantum technologies [10]. In addition, optomechanical systems have been proven to be fundamental in exemplifying the quantum-to-classical transition [11]. However, a glimpse at the underlying quantum behavior of macroscopic mechanical systems is hindered by the difficulty of cooling a mechanical mode to its quantum ground state [12]. Even for systems at cryogenic temperatures, low-frequency mechanical systems require additional cooling due to their high thermal occupation.

In the past decade, feedback [13,14] and dynamical backaction cooling [15,16] protocols have been successful in achieving ground-state cooling. The latter is based on the extraction of mechanical phonons by scattering incident drive photons to higher frequencies. This photon up-conversion (anti-Stokes) process competes with its counterpart (Stokes) process, which adds energy to the mechanical system. Dynamical backaction cooling works best in the resolved-sideband regime, where the mechanical resonant frequency exceeds the cavity decay rate $\omega_m \gg \kappa$. Within this regime, ground-state cooling using a linear cavity was achieved over a decade ago [15,16]. However, increasing the size of mechanical systems leads to a natural decrease in their frequency, which brings them into the unresolved-sideband regime $\omega_m \ll \kappa$, where Stokes and anti-Stokes processes become equally likely and hence dynamical backaction cooling becomes ineffective. Nevertheless, measurement-based feedback cooling is, in this regime, a more successful strategy [17,18], but it is limited by the imprecision of the readout [19]. Recently, this limitation was proposed to be overcome through the implementation of coherent feedback, resulting in ground-state cooling within the unresolved-sideband regime [20,21]. Moreover, multiple alternative approaches have been discussed such as using two cavity modes [22,23] or frequency-modulated light [24]. Additionally, the engineering of entirely distinct coupling mechanisms has been proposed, such as a coupling of the mechanical system to the cavity decay rate [25], an exciton polariton architecture [26], or additional two-level systems [27].

Published by the American Physical Society under the terms of the [Creative Commons Attribution 4.0 International](https://creativecommons.org/licenses/by/4.0/) license. Further distribution of this work must maintain attribution to the author(s) and the published article's title, journal citation, and DOI.

An alternative strategy to enhance cooling performance is the use of squeezed light, which can be generated either externally [28,29] or internally within the cavity [30–33]. The advantages and disadvantages of these approaches have been discussed in [34]. Such strategies are very promising but require a fine-tuning of the squeezing parameters to enable suppression of the Stokes scattering process and thus enhanced cooling. Moreover, the generation of squeezing requires a nonlinear element for the electromagnetic field, such as a χ_2 medium in the terahertz domain or Josephson-junction-based circuit loops in the microwave domain.

Interestingly, a nonlinear cavity itself can be beneficial for backaction cooling of a mechanical mode in the unresolved-sideband regime [35,36]. In this paper we analyze in detail how the nonlinearity of a Kerr resonator in a magnetomechanical architecture can be beneficial for backaction cooling of a mechanical mode. With this, we are providing the theoretical background of the analysis used in our recent experimental work Zoepfl *et al.* [37]. The latter work used a flux-mediated optomechanical coupling scheme [38–43], where a mechanical oscillator is coupled magnetically to microwave photons in a superconducting LC circuit. Here the displacement of the mechanical oscillator is converted into a magnetic flux that changes a superconducting quantum-interference device (SQUID), serving as flux-dependent inductance [35,44].

Crucially, besides being a magnetic-field-sensitive element, the SQUID is also a nonlinear element since its inductance depends on the number of photons circulating in the cavity, resulting in a typically unwanted Kerr nonlinearity within the optomechanical system. Despite limiting the driving power due to the emergence of a bistable regime, we show that a nonlinear cavity enables more efficient cooling than an identical linear system. Interestingly, the improvement in cooling performance arises particularly in the unresolved-sideband regime.

This paper is organized as follows. In Sec. II we introduce the system's Hamiltonian and study the resulting dynamics of the classical amplitude and quantum fluctuations. In Sec. III we analyze the dynamical features of the nonlinear cavity in the absence of an optomechanical interaction. In Sec. IV we turn on the interaction between the cavity and mechanical modes and demonstrate how the cavity's nonlinearity can enhance the cooling efficiency. To study the influence of the nonlinear cavity on the cooling limits, in Sec. V we derive the effective dynamics of the mechanical mode. In Sec. VI, following the work of Asjad *et al.* [28], we demonstrate that by injecting a squeezed vacuum, the unwanted backaction heating can be suppressed. Here the advantages of using a nonlinear cavity become apparent as well, as less squeezing strength is required to achieve the same level of backaction suppression if compared to an equivalent linear system. We summarize in Sec. VII.

II. MODEL

A. Hamiltonian formulation

The starting point of our discussion will be the Hamiltonian describing a mechanical oscillator parametrically coupled to a nonlinear cavity, where the latter corresponds to a Kerr

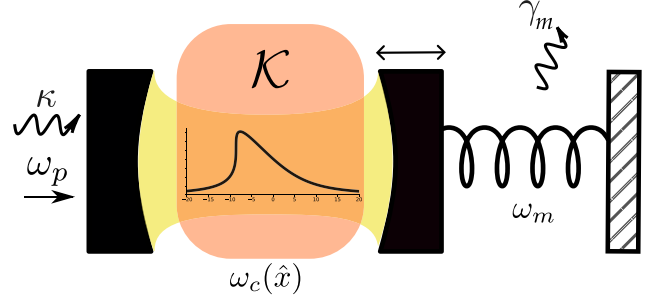


FIG. 1. Optomechanical setup consisting of a driven Kerr cavity coupled via radiation-pressure force to a mechanical resonator. Due to the presence of the nonlinearity, the average photon number circulating in the cavity exhibits a very prominent asymmetry.

resonator which can be driven into a bistable regime as depicted in Fig. 1. The Hamiltonian associated with the composite system is given as [35]

$$\hat{\mathcal{H}}_{\text{tot}} = \hat{H}_0 - \frac{\mathcal{K}}{12}(\hat{a} + \hat{a}^\dagger)^4 + \frac{g_0}{2}(\hat{a} + \hat{a}^\dagger)^2(\hat{b} + \hat{b}^\dagger) + \hat{H}_d, \quad (1)$$

where \hat{a} (\hat{b}) and \hat{a}^\dagger (\hat{b}^\dagger) are annihilating and creating an excitation in the cavity (mechanical) mode, respectively; $\hat{H}_0 = \omega_c \hat{a}^\dagger \hat{a} + \omega_m \hat{b}^\dagger \hat{b}$ denotes the free Hamiltonian of the cavity and mechanical mode, with corresponding resonance frequencies ω_c and ω_m (we set $\hbar = 1$ throughout this work); \mathcal{K} is the Kerr constant, typically assumed to be $\mathcal{K} > 0$; and $g_0 = x_{\text{ZPF}} \partial \omega_c / \partial x$ denotes the bare optomechanical coupling strength, with x_{ZPF} the zero-point-fluctuation amplitude. As $\partial \omega_c / \partial x$ cannot be directly accessed, in flux-mediated optomechanical systems it is expressed in terms of the external magnetic flux ϕ_{ext} [37,39],

$$g_0 = \frac{\partial \omega_c}{\partial \phi_{\text{ext}}} \times \frac{\partial \phi_{\text{ext}}}{\partial x} x_{\text{ZPF}}. \quad (2)$$

The first factor reflects the cavity's frequency dependence on the flux through the SQUID, enabling direct control of the coupling strength, while the second accounts for the flux variation due to the cantilever's zero-point motion. In addition, we include an external drive associated with the term $\hat{H}_d = \alpha_p e^{-i\omega_p t} \hat{a}^\dagger + \text{H.c.}$, where ω_p and α_p are the drive frequency and classical amplitude, respectively.

Furthermore, assuming a weak enough coupling g_0 and nonlinearity \mathcal{K} , the system can be simplified by neglecting counterrotating terms, yielding the time-independent Hamiltonian

$$\hat{\mathcal{H}} = -\Delta \hat{a}^\dagger \hat{a} + \omega_m \hat{b}^\dagger \hat{b} - \frac{\mathcal{K}}{2} \hat{a}^\dagger \hat{a}^\dagger \hat{a} \hat{a} + g_0 \hat{a}^\dagger \hat{a} (\hat{b} + \hat{b}^\dagger) + \hat{H}_d, \quad (3)$$

with the cavity mode rotated with respect to the drive frequency ω_p , where $\Delta = \omega_p - \omega_c$ denotes the detuning and the Hamiltonian drive term reads $\hat{H}_d = \alpha_p \hat{a}^\dagger + \text{H.c.}$

To study both classical and quantum dynamics, we introduce the so-called linearized approximation, which is based on the assumption that the system is driven strongly at the drive's frequency ω_p such that its dynamics can be well regarded as only small fluctuations in the vicinity of the

steady-state mean values. Hence, we introduce the displacement operator $\hat{D}(\eta) = \exp(\eta\hat{\delta}^\dagger - \eta^*\hat{\delta})$, with $\eta = \langle\hat{\delta}\rangle$ as an average amplitude and $\hat{\delta}$ the fluctuations around it. This allows us to transform the Hamiltonian (3) to a displaced frame of the cavity and mechanical mode. The above results in the effective description of the coherent dynamics of the fluctuations given by the Hamiltonian (see Sec. II A)

$$\begin{aligned}\hat{\mathcal{H}}_{\text{eff}} = & -\tilde{\Delta}\hat{d}^\dagger\hat{d} + \omega_m\hat{b}^\dagger\hat{b} - \frac{1}{2}(\Lambda\hat{d}^\dagger\hat{d}^\dagger + \Lambda^*\hat{d}\hat{d}) \\ & + (G\hat{d}^\dagger + G^*\hat{d})(\hat{b} + \hat{b}^\dagger),\end{aligned}\quad (4)$$

with the effective detuning $\tilde{\Delta} = \Delta + 2|\Lambda|$. This time-independent Hamiltonian is characterized by the single-mode squeezing strength $\Lambda = \mathcal{K}\bar{n}_c e^{2i\phi_c}$ and the photon-enhanced optomechanical coupling strength $G = g_0\sqrt{\bar{n}_c}e^{i\phi_c}$, with $\phi_c \in [0, 2\pi)$. Here the average coherent amplitude of the cavity field is given by $\alpha = \sqrt{\bar{n}_c}e^{i\phi_c}$, with its phase ϕ_c and the intracavity photon number \bar{n}_c .

The first two terms in $\hat{\mathcal{H}}_{\text{eff}}$ describe the modified free Hamiltonian, where the presence of the Kerr nonlinearity introduces a photon-dependent frequency shift. The third term describes a parametric amplification process induced by the Kerr nonlinearity, which plays a crucial role in squeezing generation [45]. The final term describes the usual linearized optomechanical interaction, which combines the process of swapping excitation with the process of two-mode squeezing between both modes. In the resolved-sideband regime it is possible to select either of these processes depending on the respective frequency of the drive tone. However, in the unresolved regime, both processes are contributing and in our analysis, we account for both of them.

B. Classical dynamics

To achieve a sufficiently large cooling rate, we are interested in driving strengths that lead to a large average number of intracavity photons \bar{n}_c , but at the same time do not result in multistable solutions in the classical cavity dynamics [36]. Hence, our first focus is on understanding the classical dynamics of the system. We start from the nonlinear Hamiltonian (3) and assume that the cavity is coupled to an external waveguide with rate κ . We use standard input-output theory [46] to obtain the equation of motion for the average coherent cavity amplitude α , from whose steady-state solution we can deduce the average cavity photon number (see Appendix B)

$$\bar{n}_c \left[(\Delta + \mathcal{K}_{\text{eff}}\bar{n}_c)^2 + \left(\frac{\kappa}{2}\right)^2 \right] = \kappa\bar{n}_{\text{in}}, \quad (5)$$

with the effective Kerr constant

$$\mathcal{K}_{\text{eff}} \equiv \mathcal{K} + \frac{2g_0^2\omega_m}{\omega_m^2 + \frac{\gamma_m^2}{4}} \quad (6)$$

and the input photon flux \bar{n}_{in} (in units of photons per second). The cavity and mechanical decay rates are labeled as κ and γ_m , respectively. Note that the effective Kerr equation (6) comprises both the intrinsic cavity and the optomechanically induced nonlinearities [47,48]. The latter will henceforth be referred to as the mechanical Kerr.

The average number of photons within the cavity described by the cubic equation (5) provides insight into the cavity's

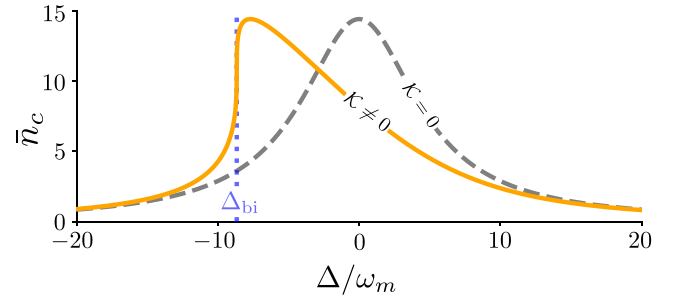


FIG. 2. Average cavity photon number as a function of the detuning $\Delta = \omega_p - \omega_c$. The orange solid line shows the intracavity photon number obtained using a nonlinear cavity ($\mathcal{K} \neq 0$) near the point of bifurcation, namely, at a drive amplitude of $\bar{n}_{\text{in}} = \bar{n}_{\text{in,crit}}$. In contrast, the gray dashed line results from the linear cavity setup ($\mathcal{K} = 0$) at the same input power. The vertical dotted line denotes the critical detuning Δ_{bi} , where the system becomes bistable.

behavior. For low drive strengths, a single real solution exists. However, for stronger drive power, a bifurcation occurs and a regime of bistability arises, where two stable states appear within a certain range of detunings. The bifurcation takes place at a point in parameter space where the first derivative of \bar{n}_c with respect to Δ diverges, which happens at a single point $\Delta = \Delta_{\text{bi}}$. Furthermore, by imposing the requirement of continuity on the transition between the two regions, we arrive at

$$\Delta_{\text{bi}} = -\frac{\sqrt{3}\kappa}{2}, \quad \bar{n}_{\text{bi}} = \frac{\kappa}{\sqrt{3}\mathcal{K}_{\text{eff}}}, \quad (7)$$

which correspond to the universal values at bifurcation. Moreover, upon substituting the relations (7) into Eq. (5), the critical drive amplitude $\bar{n}_{\text{in,bi}}$ at which bifurcation occurs can be obtained, i.e.,

$$\bar{n}_{\text{in,bi}} = \frac{\kappa^2}{3\sqrt{3}\mathcal{K}_{\text{eff}}}. \quad (8)$$

Consequently, for drive amplitudes slightly below the critical driving threshold, given by Eq. (8), the average photon number exhibits a single-valued solution with respect to the cavity detuning, with a significant gradient at Δ_{bi} , as represented by Eq. (7) and illustrated in Fig. 2. However, for the chosen parameters (see Table I), an identical linear cavity ($\mathcal{K} = 0$) driven at the same input power would show the conventional Lorentzian distribution for the average photon

TABLE I. Default values chosen for the parameters in the figures throughout the paper, if not indicated otherwise. These values are similar to those from our recent experimental work [37].

Parameter	Value
Mechanical frequency	$\omega_m/2\pi = 0.3$ MHz
Mechanical linewidth	$\gamma_m/2\pi = 0.5$ Hz
Cavity linewidth	$\kappa/2\pi = 3$ MHz
Kerr strength	$\mathcal{K}/2\pi = 0.16$ MHz
Optomechanical coupling	$g_0/2\pi = 1.7$ kHz
Input power	$\bar{n}_{\text{in,crit}} \equiv 0.999\,999\,9\bar{n}_{\text{in,bi}}$

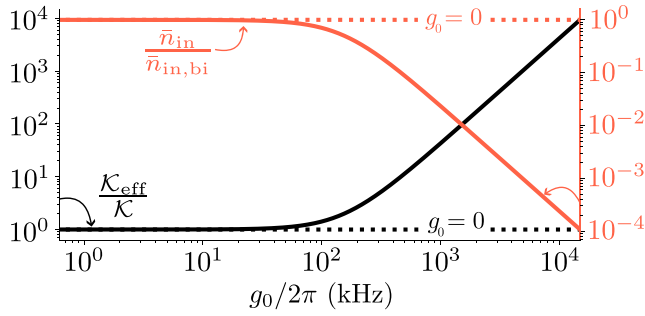


FIG. 3. The black solid line depicts the effective Kerr nonlinearity defined in Eq. (6) normalized by \mathcal{K} as a function of the optomechanical coupling strength $g_0/2\pi$. For given parameters (see Table I), the intrinsic cavity nonlinearity dominates for weak coupling strengths and the critical input power (red solid line) is dominated by \mathcal{K} . Upon increasing the coupling strength further the mechanical Kerr kicks in and the critical input power decreases as the effective Kerr is enhanced. Colored dotted lines correspond to the case without the induced mechanical Kerr, i.e., $g_0 = 0$.

number, despite the presence of the mechanical Kerr. Hence, for weak coupling strengths, the intrinsic nonlinearity of the cavity dominates over the mechanical Kerr nonlinearity, as depicted in Fig. 3.

C. Dynamics of the fluctuations

To fully understand the implications of the interaction between the mechanical and the cavity modes and thus the limit for cooling of the mechanical resonator, we analyze next the dynamics of the fluctuations. We start from the effective Hamiltonian (4) to derive the dissipative dynamics of the fluctuations described by the quantum Langevin equation

$$\frac{d}{dt}\vec{A} = \mathbf{M}\vec{A} - \mathbf{K}\vec{A}_{\text{in}}, \quad (9)$$

where we define the vector containing all mode operators $\vec{A} = [\hat{d}, \hat{d}^\dagger, \hat{b}, \hat{b}^\dagger]^T$ and the dynamical matrix \mathbf{M} as

$$\mathbf{M} = \begin{pmatrix} i\tilde{\Delta} - \frac{\kappa}{2} & i\Lambda & -iG & -iG \\ -i\Lambda^* & -i\tilde{\Delta} - \frac{\kappa}{2} & iG^* & iG^* \\ -iG^* & -iG & -i\omega_m - \frac{\gamma_m}{2} & 0 \\ iG^* & iG & 0 & i\omega_m - \frac{\gamma_m}{2} \end{pmatrix}. \quad (10)$$

In Eq. (9), the vector $\vec{A}_{\text{in}} = [\hat{d}_{\text{in}}, \hat{d}_{\text{in}}^\dagger, \hat{b}_{\text{in}}, \hat{b}_{\text{in}}^\dagger]^T$ represents the cavity and mechanical input noises, whereas the decay rates are encoded in the diagonal matrix $\mathbf{K} = \text{diag}(\sqrt{\kappa}, \sqrt{\kappa}, \sqrt{\gamma_m}, \sqrt{\gamma_m})$. The vacuum noise operator \hat{d}_{in} satisfies $\langle \hat{d}_{\text{in}}(t)\hat{d}_{\text{in}}^\dagger(t') \rangle = \delta(t-t')$ and $\langle \hat{d}_{\text{in}}^\dagger(t)\hat{d}_{\text{in}}(t') \rangle = 0$. Analogously, the noise operator \hat{b}_{in} describes coupling to a Markovian reservoir at temperature T , as represented by the correlators $\langle \hat{b}_{\text{in}}(t)\hat{b}_{\text{in}}^\dagger(t') \rangle = (\bar{n}_m^T + 1)\delta(t-t')$ and $\langle \hat{b}_{\text{in}}^\dagger(t)\hat{b}_{\text{in}}(t') \rangle = \bar{n}_m^T\delta(t-t')$. Furthermore, in the absence of any other coupling, the bath leads to the emergence of a thermal state, characterized by a mean occupation number $\bar{n}_m^T = [\exp(\omega_m/k_B T) - 1]^{-1}$ for the mechanical oscillator.

In the following sections we investigate the consequences resulting from the optomechanical interaction. This can be

accomplished by solving the linearized equations of motion in Eq. (9) in the frequency domain, from which we can deduce the relevant noise spectra and subsequently the mechanical occupation. As the response of the nonlinear cavity will determine the cavity cooling rate, we first examine the cavity in the absence of coupling to the mechanical mode.

III. NONLINEAR CAVITY

From Eq. (9) we find that in the absence of an optomechanical interaction, the dynamics of the Kerr cavity fluctuations are described by the Hamiltonian of a detuned parametric amplifier [45], yielding

$$\hat{d}[\omega] = -\sqrt{\kappa}\tilde{\mathcal{X}}_c[\omega](\hat{d}_{\text{in}}[\omega] + i\Lambda\mathcal{X}_c^*[-\omega]\hat{d}_{\text{in}}^\dagger[\omega]), \quad (11)$$

where we define the driven Kerr cavity susceptibility as

$$\tilde{\mathcal{X}}_c[\omega] = \frac{\mathcal{X}_c[\omega]}{1 - |\Lambda|^2\mathcal{X}_c[\omega]\mathcal{X}_c^*[-\omega]}, \quad (12)$$

with $\mathcal{X}_c^{-1}[\omega] = -i(\omega + \tilde{\Delta}) + \kappa/2$. The added idler noise, i.e., the second term in Eq. (11), and the modification of the cavity susceptibility will result in an asymmetric shape of the photon-number spectrum $\mathcal{S}_{nn}[\omega] = \int_{-\infty}^{\infty} dt e^{i\omega t} \langle (\hat{a}^\dagger \hat{a})(t)(\hat{a}^\dagger \hat{a})(0) \rangle$ given explicitly as (see Appendix C)

$$\mathcal{S}_{nn}[\omega] = \frac{\bar{n}_c\kappa([-\tilde{\Delta} + \omega + |\Lambda|]^2 + \frac{\kappa^2}{4})}{[\tilde{\Delta}^2 - \omega^2 + \frac{\kappa^2}{4} - |\Lambda|^2]^2 + \kappa^2\omega^2}. \quad (13)$$

The asymmetric response of the nonlinear cavity is an important characteristic for the system's ability to absorb energy. This becomes clearer when we analyze the spectrum in more detail. First we consider the poles of the spectrum, which can be extracted from the denominator of Eq. (13),

$$\Omega_{c,\pm} = -i\frac{\kappa}{2} \pm \sqrt{(\Delta + 3|\Lambda|)(\Delta + |\Lambda|)}. \quad (14)$$

Here the real (imaginary) part of the poles represents the resonance frequencies (damping rates) of the system. In Fig. 4(a) the poles are plotted as a function of the bare detuning Δ , and we can identify two distinct regions. For $\Delta < -3|\Lambda|$ and $\Delta > -|\Lambda|$ (green shaded area) the dynamics of the nonlinear cavity are governed by two resonant frequencies $\text{Re}(\tilde{\Omega}_{\pm})$ and a single decay rate, resulting in the formation of two peaks in the photon-number spectrum as shown in Fig. 4(c). On the other hand, for $-3|\Lambda| < \Delta < -|\Lambda|$ (red shaded area) the situation is reversed and the eigenvalues show degenerate imaginary parts and split dissipation rates $\text{Im}(\tilde{\Omega}_{\pm})$ as in Fig. 4(a). These two regions are delimited by exceptional points (EPs) (vertical dotted lines), which are common degeneracies in open quantum systems [49]. At an EP the system eigenvalues become degenerate and both eigenvectors coalesce due to the vanishing square root in Eq. (14). The EPs occur for the condition $\Delta_{\pm} = -(2 \pm 1)|\Lambda|$; however, the exact detuning points are not straightforwardly determined as $|\Lambda|$ is a function of the average photon number in Eq. (5), which itself depends on the detuning.

We expect that the dynamical backaction onto the mechanical mode is proportional to the variation of the photon number [35,36]; hence the steepness of the slope in the average photon

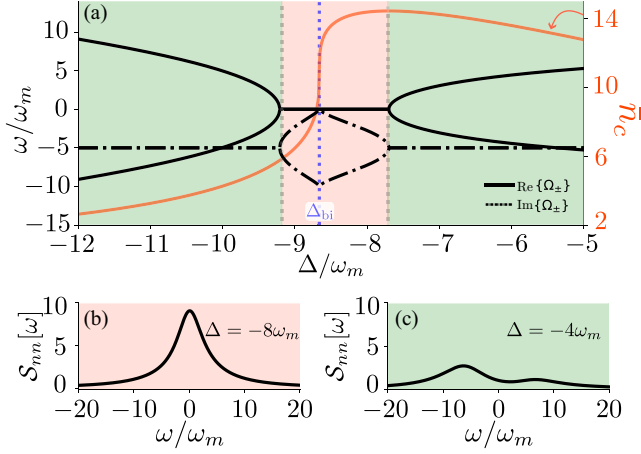


FIG. 4. (a) Poles of the driven Kerr cavity in the absence of coupling to the mechanical mode as a function of the detuning. Here we depict the real (solid line) and imaginary (dash-dotted line) parts of the poles given in Eq. (14), which are associated with the system's resonance frequency and decay, respectively. Exceptional points are shown by the vertical gray dotted lines, which delimit the interval where the system features two distinct decay rates at a single resonant frequency (red shaded area and (b)). The EPs are found at the intersection of $\Lambda = \mathcal{K}\bar{n}_c$ with the lines $-\Delta/3$ and $-\Delta$. Outside this interval, the system exhibits split resonance frequencies for a single decay rate (green shaded area) leading to a double-peak structure in the photon-number spectrum as shown in (c). Note that the decay rates' maxima and minima occur precisely at the bifurcation detuning Δ_{bi} , shown here by the vertical blue dotted line.

number [cf. the orange line in Fig. 4(a)] suggests that the relevant detuning regime for optimal cooling is the red region in Fig. 4(a). In this region, and close to the critical detuning Δ_{bi} , we observe the interesting effect that one imaginary part of the pole approaches zero, which can be interpreted as a critical slowing down of the cavity. The latter translates into a narrowing of the photon-number spectrum, reminiscent of the gain-bandwidth limitation of a parametric amplifier [50]. We deduce the exact condition for the extrema values via

$$\frac{d}{d\bar{n}_c} \text{Im}(\tilde{\Omega}_{\pm}) = 0 \Rightarrow \frac{\bar{n}_c}{\Delta} = -\frac{2}{3\mathcal{K}}, \quad (15)$$

which is equivalent to the \bar{n}_{bi} and Δ_{bi} given in Eq. (7) for $\mathcal{K}_{eff} \approx \mathcal{K}$. This indicates that, as a consequence of the cavity nonlinearity, the cavity features a minimum or maximum decay rate exactly at the critical detuning in Eq. (7), which arises due to the pronounced variation of the photon number with respect to the detuning as shown in Fig. 4(a).

However, in the detuning range enclosed by the EPs we solely have a single resonance peak at $\omega = 0$ (in this rotated frame). Crucially, changing the detuning within this range will not move the photon-number spectrum along the frequency axis, which seems to be an issue at first glance. For this we have to recall the linear case, in which the optimal detuning in the resolved-sideband regime is obtained for $\Delta = -\omega_m$ where the peak of the spectrum is located at the red sideband $\omega = \omega_m$. For a symmetric spectrum, not being able to move the spectrum in frequency space would be an issue, as no net damping could emerge. However, here is where the nonlinear

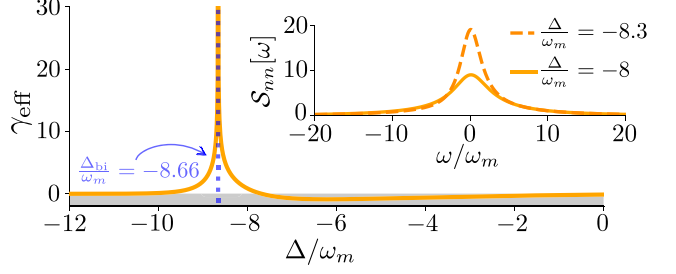


FIG. 5. Effective skewness of the photon-number spectrum of a nonlinear cavity as a function of the detuning. The inset shows the corresponding photon-number spectrum as a function of the driving frequency for detunings approaching the critical value Δ_{bi} (vertical blue dotted line). These spectra follow a slightly asymmetric Lorentzian distribution, whose maximum asymmetry is found when the cavity is driven at $\Delta = \Delta_{bi}$. Thus, as the cavity is driven close to the critical detuning, the photon-number spectrum becomes increasingly peaked and asymmetric, so for illustrative purposes we chose $\Delta = -8\omega_m$ (solid line) and $\Delta = -8.3\omega_m$ (dashed line).

response of the cavity comes into play, i.e., the asymmetry of the spectrum is essential to obtain cooling.

To quantify the asymmetry, we use the skewness, a measure which in general is utilized to characterize the asymmetry of a probability distribution. Figure 5 depicts the photon-number spectrum's effective skewness¹ γ_{eff} as a function of the cavity detuning. The maximum asymmetry occurs exactly at the critical detuning Δ_{bi} , a detuning, where we also expect the largest fluctuations due to the steepness of the slope in the average photon number (cf. Fig. 2). A positive skewness corresponds to a slightly stronger decline of the photon-number spectrum for negative frequencies and an extended tail for positive frequencies. In other words, for $\gamma_{eff} > 0$ we have $S_{nm}[\Omega] > S_{nm}[-\Omega]$, with $\Omega > 0$, which is a crucial feature for cooling the mechanics later on, as the positive (negative) frequency part of the spectrum $S_{nm}[\Omega]$ ($S_{nm}[-\Omega]$) can be interpreted as the ability of the system to absorb (emit) energy [50]. For cooling we want the cavity to absorb energy from the mechanical mode and hence a positive skewness indicates

¹Here we numerically obtained the moment-based skewness using the function $\gamma_1 = \frac{\sum_{i=1}^n (x_i - \mu)^3}{n\sigma^3}$, where x is an array of data points with length n from the distribution, and μ and σ are the mean and standard deviation of the distribution, respectively. Furthermore, since the Lorentz distribution is heavy tailed and therefore does not have finite moments, i.e., well-defined mean and variance, here we calculate the truncated moment-based skewness. This involves the data set to a finite interval, calculating the moments of the truncated distribution, and then using these moments to determine the skewness of the truncated distribution. Hence, for a certain interval of detunings Δ , we calculate the skewness of the photon-number spectrum given in Eq. (13) over a truncated set of driving frequencies ω . That means that for a $\Delta/\omega_m \in [-12, 0]$ the array x is given by the set of elements fulfilling $x = \{S_{nm}[\omega] \mid \omega/\omega_m \in [-100, 100]\}$. In addition, in Fig. 5 we show the effective skewness, which results from subtracting the constant skewness obtained using a linear cavity to the associated one of a nonlinear cavity, that is, we do $\gamma_{eff}(\Delta) = \gamma_1^{\mathcal{K} \neq 0}(\Delta) - \gamma_1^{\mathcal{K} = 0}$ with $\gamma_1^{\mathcal{K} = 0} = 3.48$.

the detuning regime of cooling. Moreover, we can already identify the required condition for the nonlinear cavity to absorb energy as

$$\mathcal{S}_{nn}[\Omega] - \mathcal{S}_{nn}[-\Omega] > 0 \quad \text{for } \Delta < -|\Lambda|. \quad (16)$$

Thus we expect that cooling will be possible for $\Delta < -|\Lambda|$, which is distinct from the linear case, which requires a negative detuning, i.e., cooling for $\Delta < 0$ if $\mathcal{K} = 0$.

In summary, the photon-number spectrum $\mathcal{S}_{nn}[\omega]$ of a nonlinear cavity deviates from the symmetric Lorentzian form of a linear cavity [3], exhibiting a fundamental asymmetry that is crucial for cooling of the mechanics. Next we will show how this nonlinearity improves cooling efficiency in the unresolved-sideband regime.

IV. DYNAMICAL BACKACTION

In the unresolved-sideband regime, where the cavity decay rate far exceeds the mechanical frequency ($\kappa \gg \omega_m$), the cavity field adapts almost instantaneously to the oscillator's position. However, when we consider the cavity's finite response time, a phase lag arises between the radiation pressure force and the mechanical motion. This retardation effect causes the force to become out of sync with the oscillator's displacement, resulting in a net energy extraction from the mechanical mode [12]. Due to the presence of the intrinsic Kerr nonlinearity, this effect is more pronounced in the interval of split decay rates (red shaded area) in Fig. 4. As a consequence of this nonlinearity, the cavity ring-down time has its maximum exactly at the point of bifurcation Δ_{bi} , as shown in Sec. III. Hence, approaching the critical detuning leads to an effective reduction of cavity linewidth, bringing the cavity into the resolved regime. However, cooling results solely from the imbalance between the Stokes and anti-Stokes processes, which is enhanced by the presence of the nonlinearity as depicted in Fig. 5.

In the weak coupling regime $g_0 \ll \kappa$, the quantum theory of optomechanical cooling can be studied within a perturbative picture [12], which is best explained in the Raman-scattering framework. Here photons from below the cavity resonance frequency are scattered upward in frequency to enter the cavity resonance, absorbing in the process a phonon from the mechanical mode. These anti-Stokes processes occur at a rate Γ_{AS} . On the other hand, the Stokes processes, where photons return redshifted through the creation of one excitation in the mechanics, happen at a rate Γ_S . Therefore, cooling can be viewed to originate from the imbalance between the Stokes and anti-Stokes scattering such that the full optomechanical damping is the net downward rate $\Gamma_{opt} = \Gamma_{AS} - \Gamma_S$.

The rates $\Gamma_{AS,S}$ can be obtained using Fermi's golden rule applied to the photon-pressure interaction between the mechanical oscillator and the photonic cavity, namely, $\hat{H}_{int} = \hat{F}\hat{x}$, with the radiation pressure force $\hat{F} = g_0\hat{a}^\dagger\hat{a}$ [50]. Hence, within the weak coupling limit, the Stokes and anti-Stokes rates are given by

$$\Gamma_{S,AS} = \mathcal{S}_{FF}[\mp\omega_m] = g_0^2 \mathcal{S}_{nn}[\mp\omega_m]. \quad (17)$$

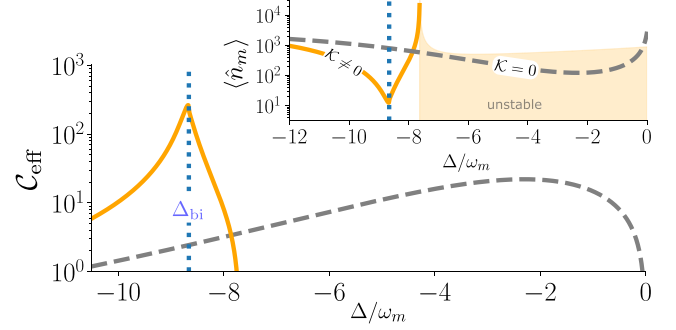


FIG. 6. Effective cooperativity as a function of the optical detuning for a nonlinear (orange solid line) and a linear (gray dashed line) cavity. Here the asymmetric shape of the photon spectrum (see Fig. 5) caused by the presence of the Kerr nonlinearity results in an increase of the cavity damping, primarily around the critical detuning. The inset shows the average phonon occupation as a function of the cavity detuning, where the minimum induced damping occurs at the point of maximum induced damping. For the parameters given in Table I, we find that the cooling capabilities of a nonlinear system outperform an equivalent but linear system by more than an order of magnitude.

With the photon-number spectrum given in Eq. (13), the optical damping becomes

$$\Gamma_{opt} = \frac{4g_0^2\bar{n}_c(|\Lambda| - \tilde{\Delta})\kappa\omega_m}{[\tilde{\Delta}^2 - \omega_m^2 + \frac{\kappa^2}{4} - |\Lambda|^2]^2 + \kappa^2\omega_m^2}, \quad (18)$$

from which we recover the cooling condition in Eq. (16), i.e., we have positive optical damping for $|\Lambda| - \tilde{\Delta} = -(\Delta + |\Lambda|) > 0$. Moreover, the expression for the optical damping indicates that a dynamical backaction evasion scheme can be realized when $\tilde{\Delta} = |\Lambda|$, which corresponds exactly to the condition of one of the EPs discussed in Sec. III. At this point the rates for heating and cooling are equal and the optical damping vanishes and the mechanics only suffer from backaction due to the fluctuations of the cavity scaling with Γ_S . This suggests that a nonlinear cavity located at the EP could be used for measurement of the oscillator's motion at the standard quantum limit [4, 19].

However, we are here interested in cooling of the mechanical mode, and thus we are aiming for maximal dynamical backaction. As discussed in Sec. III, the asymmetry of the photon-number spectrum induced by the presence of the Kerr nonlinearity produces an appreciable imbalance between the Stokes and anti-Stokes rates and consequently to an increase in the effective cooperativity $C_{eff} \equiv \Gamma_{opt}/\gamma_m$. This can be seen in Fig. 6, where the maximum cavity damping coincides with the point of maximum asymmetry, at Δ_{bi} , where the cavity ring-down time is maximized. At this bifurcation point, the circulating photon number within the nonlinear cavity exhibits a significant variation, thereby enhancing the cooling process [37].

It has been proposed that intracavity squeezing can be utilized to remove the backaction onto the mechanical mode [30–33], i.e., by achieving $\Gamma_S = 0$. This procedure requires a careful matching of the optomechanical interaction and

squeezing strengths in their magnitude and, most importantly, in their phase. Here we have a single phase that originates from the cavity amplitude ϕ_c and which enters our coherent dynamics in Eq. (4). This phase can be gauged away and hence we have no phase independence of our optomechanical and squeezing processes. This prevents us from using it for the suppression of the unwanted backaction heating. However, as we will study later, injecting squeezed vacuum light into the cavity can be employed to suppress the Stokes rate given in Eq. (17), thereby allowing the system to surpass the backaction limit in its cooling capabilities [28].

V. COOLING

In order to investigate the limits of cooling in our setup, we analyze the influence of the nonlinear cavity on the dynamics of the mechanical mode by deriving the effective average mechanical occupation. For this we solve the equations of motion (9) for the b mode to find an effective dynamical description of the mechanical oscillator. Defining the vector $\vec{\mathbf{B}}[\omega] = [\hat{b}[\omega], \hat{b}^\dagger[\omega]]^T$, we obtain

$$\chi_{m,\text{eff}}^{-1}[\omega] \vec{\mathbf{B}}[\omega] = -\sqrt{\gamma_m} \vec{\mathbf{B}}_{\text{in,eff}}[\omega], \quad (19)$$

with $\vec{\mathbf{B}}_{\text{in,eff}}[\omega] = [\hat{B}_{\text{in}}[\omega], \hat{B}_{\text{in}}^\dagger[\omega]]^T$ containing the modified noise impinging on the mechanical mode,

$$\hat{B}_{\text{in}}[\omega] = \hat{b}_{\text{in}}[\omega] + \frac{i}{\sqrt{\gamma_m}} [\eta[\omega] \hat{d}_{\text{in}}^\dagger[\omega] + \eta^*[-\omega] \hat{d}_{\text{in}}[\omega]], \quad (20)$$

with the coefficient

$$\eta[\omega] = -\frac{\sqrt{\kappa}}{\mathcal{N}[\omega]} (G \chi_c^{-1}[\omega] + i G^* \Lambda), \quad (21)$$

where we introduced $\mathcal{N}[\omega] = \chi_c^{*-1}[-\omega] \chi_c^{-1}[\omega] - |\Lambda|^2$. Additionally, the response of the mechanical mode is encoded in the susceptibility matrix

$$\chi_{m,\text{eff}}^{-1}[\omega] = \begin{pmatrix} \chi_m^{-1}[\omega] - i \Sigma_c[\omega] & -i \Sigma_c[\omega] \\ i \Sigma_c[\omega] & \chi_m^{*-1}[-\omega] + i \Sigma_c[\omega] \end{pmatrix}, \quad (22)$$

with the cavity self-energy

$$\Sigma_c[\omega] \equiv \frac{2|G|^2(|\Lambda| - \tilde{\Delta})}{(-i\omega + \frac{\kappa}{2})^2 + \tilde{\Delta}^2 - |\Lambda|^2} \quad (23)$$

and the mechanical susceptibility $\chi_m^{-1}[\omega] = -i(\omega - \omega_m) + \gamma_m/2$. Due to the optomechanical interaction, the effective susceptibility in Eq. (22) contains the modified mechanical frequency and damping rate $\omega_m - \text{Re}(\Sigma_c[\omega])$ and $\gamma_m + 2 \text{Im}(\Sigma_c[\omega])$, respectively. In addition to the frequency shift $\text{Re}(\Sigma_c[\omega])$ and the damping $\text{Im}(\Sigma_c[\omega])$, the cavity also induces single-mode squeezing in the mechanical oscillator with effective coupling strength $\Sigma_c[\omega]$. As pointed out before, a cancellation of dynamical backaction can be achieved when the nonlinear cavity is located at the EP $\tilde{\Delta} = |\Lambda|$, meaning that the cavity self-energy $\Sigma_c[\omega]$ vanishes. In contrast, if a linear cavity is employed, an equivalent effect arises on resonance $\Delta = 0$.

For sufficient weak coupling $\kappa \gg g_0$, the cavity self-energy can be evaluated at the mechanical resonance frequency, namely, $\Sigma_c[\omega] \approx \Sigma_c[\omega_m]$. Hence, assuming a high- Q mechanical oscillator, the mechanical noise spectrum takes the rather simple form

$$\begin{aligned} \mathcal{S}_{bb}[\omega] = & \frac{\gamma_m |\chi_m^{*-1}[-\omega] + i \Sigma_c[\omega_m]|^2}{|(\omega - \Omega_{m,+})(\omega - \Omega_{m,-})|^2} \bar{n}_m^T \\ & + \frac{\gamma_m |\Sigma_c[\omega_m]|^2}{|(\omega - \Omega_{m,+})(\omega - \Omega_{m,-})|^2} (\bar{n}_m^T + 1) \\ & + \frac{|\chi_m^{*-1}[-\omega]|^2}{|(\omega - \Omega_{m,+})(\omega - \Omega_{m,-})|^2} \Gamma_s, \end{aligned} \quad (24)$$

with the poles $\Omega_{m,\pm} = -i\gamma_m/2 \pm \sqrt{\omega_m^2 - 2\omega_m \Sigma_c[\omega_m]}$ and the Stokes rate given by Eq. (17). The first two terms in the final expression represent the modified mechanical noise contributions, which are associated with both the thermal and vacuum fluctuations of the oscillator's mode. Note that the contribution proportional to $\bar{n}_m^T + 1$ arises exclusively due to the optomechanical interaction yielding the squeezing of the mechanics. Finally, the final term represents the cavity backaction noise, which originates solely from the interaction with the cavity and contributes an additional source of noise.

The average occupation of the mechanical mode can be obtained via the integration of the mechanical noise spectrum

$$\langle \hat{n}_m \rangle = \int \frac{d\omega}{2\pi} \mathcal{S}_{bb}[\omega], \quad (25)$$

with the noise spectrum given in Eq. (24). Since for the current parameters we have $\Sigma_c[\omega_m]/\omega_m \ll 1$, the integral can be solved analytically. The above implies that the off-diagonal elements of the effective mechanical susceptibility given in Eq. (22) can be neglected and with this, the induced squeezing, described by nonresonant processes.

Using Eq. (25) and assuming a high- Q mechanical oscillator, we can approximate the average mechanical occupation as

$$\langle \hat{n}_m \rangle \approx \frac{\bar{n}_m^T}{\mathcal{C}_{\text{eff}} + 1} + \frac{\mathcal{C}_{\text{eff}}}{\mathcal{C}_{\text{eff}} + 1} \frac{(\omega_m - \Delta_{\text{eff}})^2 + \frac{\kappa^2}{4}}{4\omega_m \Delta_{\text{eff}}}, \quad (26)$$

with the detuning $\Delta_{\text{eff}} \equiv |\Lambda| - \tilde{\Delta}$. The first term in Eq. (26) corresponds to a modified thermal occupation, whereas the second term comes from the unwanted cavity backaction heating. Note that in the absence of optomechanical interaction, the mechanical occupation is on average its thermal occupation, i.e., \bar{n}_m^T .

An equivalent description of the cooling, as indicated in Sec. IV, is provided by an effective master equation for the mechanical mode, which results in the steady-state average mechanical occupation (see Appendix F)

$$\langle \hat{n}_m \rangle_s = \frac{\gamma_m \bar{n}_m^T}{\gamma_m + \Gamma_{\text{opt}}} + \frac{\Gamma_s}{\gamma_m + \Gamma_{\text{opt}}}, \quad (27)$$

with the Stokes and anti-Stokes rates given by Eq. (17). Thus, the substitution of Eq. (17) into Eq. (27) coincides with the approximate result obtained in Eq. (26). From Eq. (26) we find that for high effective cooperativity, the minimal phonon

number is set by the cavity backaction, yielding

$$\bar{n}_{\text{BA}} \equiv \lim_{C_{\text{eff}} \rightarrow \infty} \langle \hat{n}_m \rangle = \frac{(\omega_m - \Delta_{\text{eff}})^2 + \frac{\kappa^2}{4}}{4\omega_m \Delta_{\text{eff}}}, \quad (28)$$

which by replacing $\Delta_{\text{eff}} \rightarrow -\Delta$ coincides with the expression of the lowest achievable phonon number if a linear cavity is employed [3]. Hence, the ultimate cooling limit is imposed by the cavity backaction just as in the linear case. However, we can still determine the optimal detuning in Eq. (28) as $\Delta_{\text{eff}} \rightarrow \sqrt{\kappa^2/4 + \omega_m^2}$, which minimizes \bar{n}_{BA} , yielding $\bar{n}_{\text{BA}}^{\text{min}} = (\sqrt{\kappa^2/\omega_m^2 + 4} - 2)/4$. Thus, ground-state cooling, i.e., $\bar{n}_{\text{BA}}^{\text{min}} < 1$, is only possible when $\omega_m/\kappa > (4\sqrt{2})^{-1} \approx 0.177$, which coincides with the case of a linear cavity.

A high effective cooperativity enables in particular the suppression of the thermal occupation, as we see from the first term of Eq. (26). Operating below the bifurcation point of the nonlinear cavity, the driving strength is constrained, and with the given parameters, we can reach an effective cooperativity of $C_{\text{eff}} \approx 264$, as shown in Fig. 6. In contrast, for equivalent parameters and driving strength, a linear cavity achieves an effective cooperativity of only $C_{\text{eff}} \approx 22$. This demonstrates that, under the given conditions, the use of a nonlinear cavity leads to an improvement of an order of magnitude in cooling performance. To reach a comparable cooling limit, a linear cavity would require nearly 12 times more input power. This is feasible because the linear system is not limited by the drive power in the same way as a nonlinear cavity. Nevertheless, this highlights the superior cooling efficiency of a nonlinear cavity compared to a linear cavity at low input powers.

With the parameters given in Table I the mechanical occupation can be suppressed from 2778 thermal phonons down to $\langle \hat{n}_m \rangle = 12.66$, which is about 220 times lower than the thermal occupation. This result agrees with the cooling performance demonstrated experimentally in [37], which used similar parameters. According to Eq. (26), this remaining occupation consists of the modified thermal and backaction contributions, with the latter accounting for 2.74 phonons. In contrast, with the same parameters and identical input power, a linear cavity achieves a cooling limit of 123.33 phonons, as depicted in the inset of Fig. 6. Additionally, it is also worth noting the possibility to operate above bifurcation as in the work of Deeg *et al.* [51].

We now loosen up the constraints imposed by the parameters given in Table I and explore the lowest phonon occupation reached with the nonlinear setup as we increase the optomechanical coupling strength. The minimum phonon number, depicted in Fig. 7, is achieved by optimizing the input power for each optomechanical coupling strength, with the constraint that the system remains in the monostable regime. Moreover, for larger coupling strengths the thermal contribution can be suppressed more efficiently, and optimal input power then means to work with a lower power value to reduce the backaction. The nonlinear setup allows cooling down to $\langle \hat{n}_m \rangle = 2.26$ for a coupling strength of $g_0/2\pi = 23.28$ kHz, which represents a 26% improvement over the linear setup for identical parameters yielding $\langle \hat{n}_m \rangle = 3.06$ (not shown in the graph). Within the chosen range of input powers the linear minimum can be further suppressed down to 2.41 phonons by increasing the coupling strength significantly. Thus, cooling

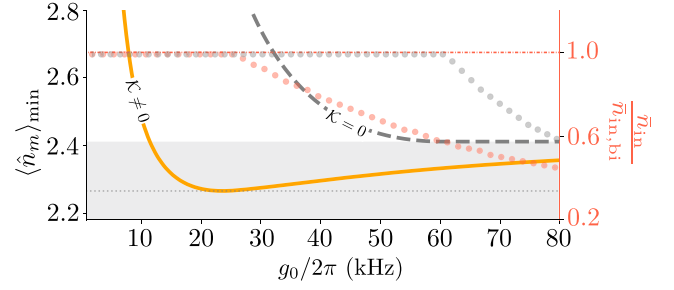


FIG. 7. Lowest phonon number reached as a function of the optomechanical coupling strength. The use of a nonlinear cavity (orange solid line) outperforms an identical but linear setup (gray dashed line) even for weaker coupling strengths. For each value of coupling strength, we have used the optimal input power below bifurcation (red and gray dotted lines for $\mathcal{K} \neq 0$ and $\mathcal{K} = 0$, respectively). Note that the optimal input power drops down for larger coupling strengths, minimizing the backaction contribution. The gray shaded region shows the minimal phonon occupation reached for large g_0 in the linear case. The remaining parameters are as given in Table I.

with a linear cavity requires a larger optomechanical coupling strength or a substantial increase in the input power. In contrast, the nonlinear setup provides a more efficient cooling at lower g_0 even exceeding the linear minimum of 2.41 phonons. However, for the parameters given in Table I, the minimum backaction $\bar{n}_{\text{BA}}^{\text{min}} \approx 2.049$ is only possible with a linear cavity, since it has no bifurcation constraints. Nevertheless, reaching this limit requires for, e.g., $g_0/2\pi = 15$ kHz a substantial increase in power strength of $\bar{n}_{\text{in}} \approx 10^2 \bar{n}_{\text{in,bi}}$.

To further study the benefits of the nonlinear setup, we analyze the lowest mechanical occupation achieved as a function of the resolved parameter ω_m/κ . In Fig. 8 we compare the cooling performance of the nonlinear with the conventional linear system for fixed $g_0/2\pi = 15$ kHz and both equally driven at $\bar{n}_{\text{in}} = \bar{n}_{\text{in,crit}}$. For this optomechanical coupling strength, the mechanical occupation reached using the nonlinear cavity lies close to the minimum phonon number provided by the cavity backaction (blue shaded area). In contrast, the linear system does not reach the backaction limit for the given input power. Remarkably, we find that the more

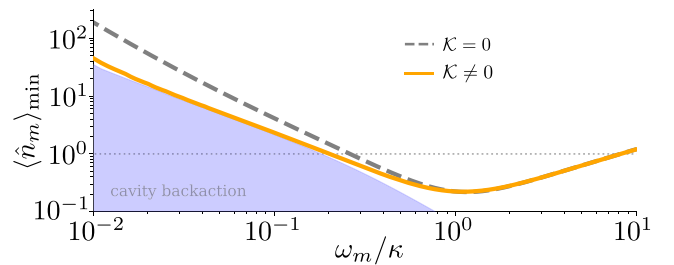


FIG. 8. Lowest phonon occupation as a function of the resolved-sideband parameter ω_m/κ . In the unresolved-sideband regime, the nonlinear cavity (orange solid curve) achieves better cooling performance compared to a linear cavity (gray dashed curve) at the same input power. For the given parameters, with an optomechanical coupling strength of $g_0/2\pi = 15$ kHz, the mechanical occupation is constrained by the cavity's backaction (blue shaded area).

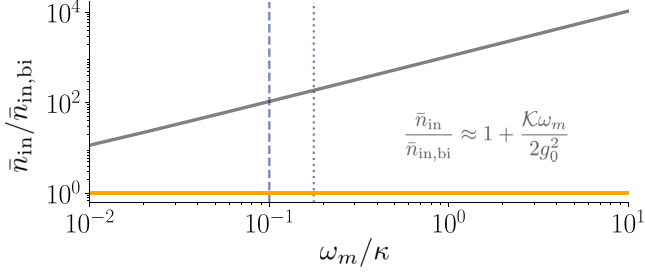


FIG. 9. Required input power for optimal cooling as a function of the resolved-sideband parameter ω_m/κ . A linear cavity (gray solid line) operating in the monostable requires substantially more input power to reach the backaction limit compared to a nonlinear system (orange solid line). The vertical dashed line represents experimental parameters, while the vertical dotted line marks the resolved-sideband parameter from which ground-state cooling becomes feasible. In addition to the given parameters, the optomechanical coupling strength $g_0/2\pi = 15$ kHz.

unresolved our system is, the better our improvement will be using a nonlinear cavity. However, as we approach the resolved-sideband regime the advantage of the nonlinear setup diminishes, showing results similar to those for the linear system. As expected from our discussion of the backaction limit below Eq. (28), for a resolved-sideband parameter of around $\omega_m/\kappa \approx 0.2$, an occupation below one is achieved. A linear system requires here a similar value, but notably the ratio g_0/κ has to be roughly twice as high for the same input power (see Appendix G for further details). Note that for $\omega_m/\kappa > 1$ we observe an increase in temperature because the driving power for the linear case is not optimized. In contrast, for the nonlinear setup, the temperature increase is constrained by the critical input power.

So far we have mainly focused on a comparison with an equally strong driven linear cavity, highlighting the improved performance of a nonlinear setup in the unresolved-sideband regime. However, by driving stronger, a linear cavity can in general reach the backaction limit. In Fig. 9 we show the required input power for such an optimal cooling. It becomes apparent that substantially more input power is required for the linear setup. Restricting the linear cavity to the monostable regime, i.e., to powers below the bistable regime induced by the mechanical Kerr, we find that the optimal input power is at $\bar{n}_{\text{in}} = 0.99\bar{n}_{\text{in,bi}}^{\mathcal{K}=0}$ and with Eq. (8) we obtain

$$\frac{\bar{n}_{\text{in}}}{\bar{n}_{\text{in,bi}}} \approx \frac{\bar{n}_{\text{in,bi}}^{\mathcal{K}=0}}{\bar{n}_{\text{in,bi}}} = 1 + \frac{\mathcal{K}}{\mathcal{K}_m} \approx 1 + \frac{\mathcal{K}\omega_m}{2g_0^2}, \quad (29)$$

where we use the definition of the mechanical Kerr in Eq. (6) in the last step. Thus, the input power exhibits a linear dependence with the mechanical frequency.

Figure 8 also makes clear that deep in the unresolved-sideband regime there is no way around the cavity backaction. Here alternative protocols are required, utilizing, for example, feedback or squeezing. In the next section we provide a pathway towards the ground state utilizing the squeezing tactic for our nonlinear setup, following the linear protocol developed by Asjad *et al.* [28].

VI. TOWARDS THE GROUND STATE

In Sec. V we demonstrated that in the unresolved-sideband regime a nonlinear cavity outperforms a linear system in its efficiency. Nevertheless, despite this improvement, cooling to the ground state is still constrained by the cavity backaction as shown in Fig. 8. To overcome this limitation and cool below the backaction limit, the use of, for example, optomechanically induced transparency [52] and pulsed cooling schemes [53], has been proposed. Alternatively, the use of squeezing, generated inside or outside the cavity, has been studied to improve the cooling performance in an optomechanical system [28,29,34,54,55]. In this section we discuss how such a squeezing approach is straightforwardly transferable to the nonlinear system. Following [28], we show that driving a nonlinear optomechanical cavity with a squeezed vacuum allows us to suppress the Stokes process and thereby strongly reduce the unwanted cavity backaction.

Formally, pure squeezed states arise through the action of the squeezing operator $\hat{S}(r) = \exp(re^{i\theta}\hat{a}^2/2 + \text{H.c.})$ onto the vacuum state of a bosonic mode \hat{a} , where $r \in [0, \infty)$ and $\theta \in [0, 2\pi]$ denote the squeezing strength and angle, respectively. Experimentally, squeezed states can be generated by injecting a vacuum into a degenerate parametric amplifier (DPA) [45,56]. Assuming that the output of the DPA is cascaded into the optomechanical system yields the new cavity noise operators

$$\begin{aligned} \langle \hat{d}_{\text{in}}^\dagger(t) \hat{d}_{\text{in}}(t') \rangle &= \xi N_s \delta(t - t'), \\ \langle \hat{d}_{\text{in}}(t) \hat{d}_{\text{in}}(t') \rangle &= \xi M_s e^{-2i\varphi} \delta(t - t'), \end{aligned} \quad (30)$$

where

$$N_s = \frac{(\kappa_+^2 - \kappa_-^2)^2}{4\kappa_+^2\kappa_-^2}, \quad M_s = \frac{\kappa_+^4 - \kappa_-^4}{4\kappa_+^2\kappa_-^2}, \quad (31)$$

with $\kappa_{\pm} = \kappa/2 \pm |\chi|$, where we utilize $\chi = |\chi|e^{-2i\varphi}$ as the squeezing parameter and φ as the squeezing angle (see Appendix H for details). Furthermore, we introduce a scaling parameter ξ which accounts for intrinsic losses in the system; this parameter quantifies how effectively the squeezed vacuum is produced and routed towards the nonlinear cavity. We refer to this parameter as the purity of the squeezing as $\xi = 1$ denotes pure squeezing and $\xi = 0$ vacuum noise only. Note that for the latter case the noise correlators in Eq. (30) vanish, as expected for a vacuum. Using these correlators, we can derive the radiation pressure force spectrum $\mathcal{S}_{FF}[\omega]$ (the explicit expression can be found in Appendix H). From the force spectrum we can extract the total damping rate $\Gamma_{\text{tot}} = \mathcal{S}_{FF}[\omega_m] - \mathcal{S}_{FF}[-\omega_m]$ and determine the cavity backaction limit $\bar{n}_{\text{BA}} = \Gamma_s/\Gamma_{\text{tot}}$. Note that the total damping rate Γ_{tot} is independent of the input squeezed light and therefore cannot be used to improve the cooling performance. Nevertheless, we can still minimize the Stokes process and consequently reduce the cavity backaction by choosing the optimal squeezing phase obtained from $d/d\varphi$, $\Gamma_s = 0$. Using this optimal squeezing phase, the cavity backaction becomes

$$\bar{n}_{\text{BA}}^s = \bar{n}_{\text{BA}} \left[1 + \left(1 + \frac{1}{\wp^2} \right) \xi N_s - \frac{2\xi M_s}{\wp} \right], \quad (32)$$

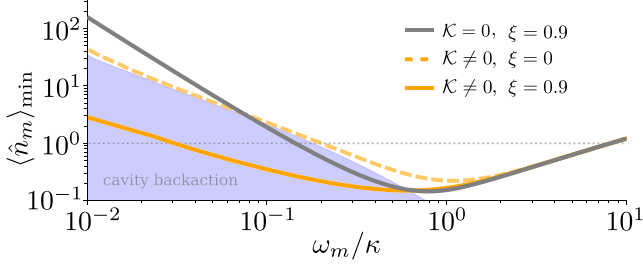


FIG. 10. Lowest phonon occupation as a function of the resolved-sideband parameter ω_m/κ at $g_0/2\pi = 15$ kHz. A nonlinear cavity driven with only vacuum noise (orange dashed line) is limited by the unwanted cavity backaction, which can be suppressed when a squeezed vacuum enters the cavity (orange solid line). This suppression is also observed for the linear case for the same parameters (gray solid line), but is less successful in comparison to the nonlinear case, an advantage of the nonlinear system which decreases as ω_m increases.

with \bar{n}_{BA} given by Eq. (28) and

$$\wp^2 = \frac{[\Delta_{\text{eff}} - \omega_m]^2 + \frac{\kappa^2}{4}}{[\Delta_{\text{eff}} + \omega_m]^2 + \frac{\kappa^2}{4}}. \quad (33)$$

We can minimize the backaction in Eq. (32) over the squeezing parameter incorporated in N_s and find that for $\wp = \sqrt{N_s/(N_s + 1)}$ we obtain

$$\bar{n}_{\text{BA}}^s = \bar{n}_{\text{BA}}(1 - \xi). \quad (34)$$

As expected, in the absence of squeezing we recover Eq. (28), but for $\xi = 1$ we can fully suppress the unwanted cavity backaction. In Fig. 10 we show the lowest phonon number achieved when a squeezed vacuum is injected into the cavity. As explained before, the injected squeezing results in the possibility of suppressing the Stokes scattering process, thus reducing the cavity backaction heating. In this way, the use of a squeezed input allows us to exceed the cooling limits obtained when only vacuum noise enters the nonlinear cavity. This improvement is also appearing when a squeezed vacuum is injected into a linear cavity, as depicted by the gray solid line in Fig. 10. However, as in Sec. V, in the unresolved-sideband regime a nonlinear cavity outperforms an equivalent linear system when both are equally driven. Furthermore, for a nonlinear cavity at $g_0/2\pi = 15$ kHz with $\xi = 0.9$, ground-state cooling is achieved for $\omega_m/\kappa = 0.03$, whereas for a linear cavity it requires $\omega_m/\kappa = 0.144$, which demonstrates again the benefits of a nonlinear cavity in the unresolved-sideband regime.

Alternatively, one can ask about the squeezing requirements to achieve a mechanical occupation below one in the linear versus nonlinear case. To discuss this we fix the coupling strength to $g_0/2\pi = 15$ kHz and choose the resolved-sideband parameter as $\omega_m/\kappa = 0.13$. As indicated by the two black dots in Fig. 11, we find that by using a squeezed vacuum with $\xi = 0.99$ for the linear cavity, the unwanted cavity backaction is sufficiently suppressed, allowing the linear case to reach an occupation below one at $\omega_m/\kappa = 0.13$. We can connect the required amount of squeezing via $\xi N_s \equiv \sinh^2(r)$ to an effective squeezing strength of

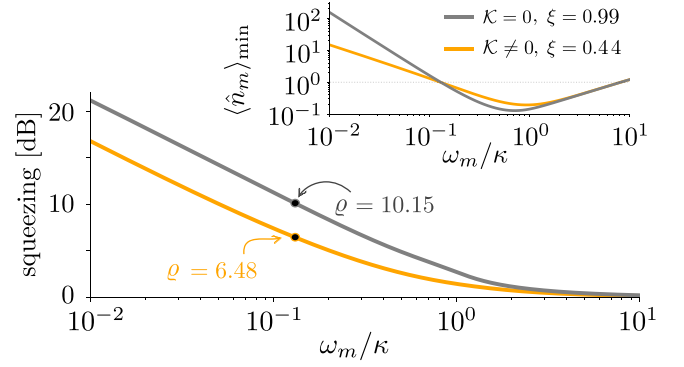


FIG. 11. Squeezing for optimal cooling as a function of the resolved-sideband parameter for the nonlinear (orange line) and the linear (gray line) case, using a purity of squeezing of $\xi = 0.44$ and 0.99 , respectively. The two black dots denote the respective squeezing strengths at $\omega_m/\kappa = 0.13$ discussed in the text. The inset shows the corresponding minimum phonon number as a function of the resolved parameter. Here mechanical occupation below one is obtained at $\omega_m/\kappa = 0.13$, where both lines intersect. For the plots we used $g_0/2\pi = 15$ kHz and the remaining parameters are as in Table I.

$\varrho = 10 \log_{10} e^{2r} = 10.15$ dB to achieve these results (see Appendix H). In contrast, under the same parameters, a nonlinear cavity requires lower purity ($\xi = 0.44$) and thus lower squeezing strength ($\varrho = 6.48$ dB) than a linear cavity to achieve equivalent cooling limits. This highlights the superior cooling efficiency of a nonlinear cavity compared to a linear system in the unresolved-sideband regime, as visible in Fig. 11, which depicts the requirements on the squeezing strength as a function of the resolved-sideband parameter. Note that for increasing the sideband resolved parameter, best cooling arises when $\Delta_{\text{eff}} \approx \omega_m$. From Eq. (33) the above results in $\wp^2 \rightarrow 0$, leading to a vanishing squeezing strength. Additionally, when approaching the resolved-sideband regime, the cooling benefits of the nonlinear cavity diminish. This regime is also not limited by the backaction of the cavity; hence the squeezing protocol loses its benefit.

VII. CONCLUSION

In summary, in this work we showed that a nonlinear cavity, which is dispersively coupled to a low-frequency mechanical oscillator, is more efficient in dynamical backaction cooling compared to an identical linear system. More efficient means that for achieving low occupations in the unresolved-sideband regime, the requirements on optomechanical coupling strengths and driving power are significantly lower in the nonlinear case.

We illustrated that the nonlinear nature of the cavity is crucial in the description of the optomechanical backaction. In this regard, the description of the classical dynamics is vital in this study, since the strongest cooling appears at the point of bifurcation of the classical cavity dynamics. We showed that this enhanced cooling performance results from the distinctive asymmetric photon-number spectrum of the nonlinear cavity. Moreover, we found that the limits for dynamical backaction cooling coincide in the linear and nonlinear cases. However,

when driven with a squeezed vacuum to mitigate the unwanted backaction heating, a nonlinear cavity demonstrates again superior cooling efficiency. For identical parameters, ground-state cooling with a nonlinear cavity demands considerably less squeezing strength than a linear system, which is very intriguing from an experimental perspective.

Despite being considered separately as unwanted features, the combination of an optomechanical system in the unresolved-sideband regime with an intrinsically nonlinear cavity leads to a better cooling performance. This makes the nonlinear cavity an appealing system for applications involving large and thus low-frequency mechanical systems.

ACKNOWLEDGMENTS

We want to thank Hans Huebl, John Teufel, and Witlef Wieczorek for fruitful discussions. N.D.-N. and A.M. acknowledge funding through Project No. CRC 183. A.M. acknowledges funding from the Deutsche Forschungsgemeinschaft through the Emmy Noether program (Grant No. ME 4863/1-1). D.Z. was funded by the European Union's Horizon 2020 research and innovation program under Grant Agreements No. 736943 and No. 101080143. M.L.J. acknowledges funding from the NSERC and the Canada First Research Excellence Fund. C.M.F.S. and L.D. were supported by the Austrian Science Fund (FWF) [Grant DOI: 10.55776/W1259]. This work was supported by the European Union's Horizon Europe 2021–2027 Framework Programme under Grant Agreement No. 101080143 (SuperMeQ).

APPENDIX A: DERIVATION OF THE EFFECTIVE HAMILTONIAN

The dynamics of the system can be analyzed within the framework of the master equation, in which the cavity is considered as a reservoir responsible for inducing both heating and cooling processes in the mechanical mode, specifically referred to as Stokes and anti-Stokes processes, respectively. The master equation reads

$$\frac{d}{dt}\hat{\rho} = -i[\hat{\mathcal{H}}, \hat{\rho}] + \kappa\hat{\mathcal{D}}[\hat{a}]\hat{\rho} + \gamma_m(\bar{n}_m^T + 1)\hat{\mathcal{D}}[\hat{b}]\hat{\rho} + \gamma_m\bar{n}_m^T\hat{\mathcal{D}}[\hat{b}^\dagger]\hat{\rho}, \quad (\text{A1})$$

where $\hat{\rho} \in \mathcal{H}_c \otimes \mathcal{H}_m$ is the density operator of the composite system, with $\mathcal{H}_{c(m)}$ the Hilbert space of the optical (mechanical) mode; $\hat{\mathcal{H}}$ is the Hamiltonian in Eq. (3); and $\hat{\mathcal{D}}[\hat{\rho}]\bullet = \hat{\rho}\bullet\hat{\rho}^\dagger - \{\hat{\rho}^\dagger\hat{\rho}, \bullet\}/2$, with \bullet a placeholder.

Recalling the displacement operator for the cavity mode $\hat{D}(\alpha) = \exp(\alpha\hat{a}^\dagger - \alpha^*\hat{a})$ and the Baker-Hausdorff formula [57], we find that $\hat{D}^\dagger(\alpha)\hat{a}\hat{D}(\alpha) = \alpha + \hat{a}$, with the time-dependent classical amplitude $\alpha = \alpha(t)$. Similarly, we introduce the displacement operator for the mechanical $\hat{D}^\dagger(\beta)$, whose action yields $\hat{D}^\dagger(\beta)\hat{b}\hat{D}(\beta) = \beta + \hat{b}$, where the time-dependent classical amplitude $\beta = \beta(t)$ and, for simplicity, we kept the operator \hat{b} to describe the fluctuations in the mechanics.

We now continue transforming Eq. (A1) to a displaced frame $\hat{\rho} \rightarrow \hat{\rho}' = \hat{P}\hat{\rho}\hat{P}^\dagger$ with the unitary $\hat{P}(t) = \hat{D}^\dagger(\alpha)\hat{D}^\dagger(\beta)$,

which results in

$$\begin{aligned} \frac{d}{dt}\hat{\rho}' = & -i[\hat{\mathcal{H}}', \hat{\rho}'] + \kappa\hat{\mathcal{D}}[\alpha + \hat{a}]\hat{\rho}' \\ & + \gamma_m(\bar{n}_m^T + 1)\hat{\mathcal{D}}[\beta + \hat{b}]\hat{\rho}' + \gamma_m\bar{n}_m^T\hat{\mathcal{D}}[\beta^* + \hat{b}^\dagger]\hat{\rho}', \end{aligned} \quad (\text{A2})$$

with the transformed Hamiltonian

$$\hat{\mathcal{H}}' = \hat{P}(t)\hat{\mathcal{H}}\hat{P}^\dagger(t) + i\frac{\partial\hat{P}(t)}{\partial t}\hat{P}^\dagger(t). \quad (\text{A3})$$

Here the second term does not vanish due to the time dependence of the classical mode amplitudes, and using the product rule it follows that

$$i\frac{\partial\hat{P}(t)}{\partial t}\hat{P}^\dagger(t) = -i\left(\frac{\partial\alpha}{\partial t}\hat{a}^\dagger - \frac{\partial\alpha^*}{\partial t}\hat{a}\right) - i\left(\frac{\partial\beta}{\partial t}\hat{b}^\dagger - \frac{\partial\beta^*}{\partial t}\hat{b}\right). \quad (\text{A4})$$

To find the transformed Hamiltonian in Eq. (A3), we recall the analysis done in Sec. II B yielding the explicit expression for the dynamics of the cavity amplitude

$$\frac{d}{dt}\alpha = \left(i\Delta - \frac{\kappa}{2}\right)\alpha + i\mathcal{K}|\alpha|^2\alpha - i\frac{g_0}{x_{\text{ZPF}}}(\hat{x})\alpha - i\alpha_p, \quad (\text{A5})$$

where $\langle\hat{x}\rangle = x_{\text{ZPF}}\langle\hat{b} + \hat{b}^\dagger\rangle$. Analogously, for the mechanics we find

$$\frac{d\beta}{dt} = -\left(i\omega_m + \frac{\gamma_m}{2}\right)\beta - ig_0|\alpha|^2. \quad (\text{A6})$$

The substitution of Eqs. (A5) and (A6) into Eq. (A3) using Eq. (A4) leads us to the effective description of the master equation

$$\begin{aligned} \frac{d}{dt}\hat{\rho}' = & -i[\hat{\mathcal{H}}', \hat{\rho}'] + \kappa\hat{\mathcal{D}}[\hat{d}]\hat{\rho}' \\ & + \gamma_m(\bar{n}_m^T + 1)\hat{\mathcal{D}}[\hat{b}]\hat{\rho}' + \gamma_m\bar{n}_m^T\hat{\mathcal{D}}[\hat{b}^\dagger]\hat{\rho}', \end{aligned} \quad (\text{A7})$$

with the modified Hamiltonian

$$\begin{aligned} \hat{\mathcal{H}}' = & -\left(\Delta + 2\mathcal{K}|\alpha|^2 - \frac{g_0}{x_{\text{ZPF}}}\langle\hat{x}\rangle\right)\hat{d}^\dagger\hat{d} + \omega_m\hat{b}^\dagger\hat{b} \\ & - \frac{\mathcal{K}}{2}(\alpha^2\hat{d}^{2\dagger} + \alpha^{*2}\hat{d}^2) + g_0[\alpha^*\hat{d} + \alpha\hat{d}^\dagger][\hat{b} + \hat{b}^\dagger] + \hat{\mathcal{H}}_{\text{NL}}, \end{aligned} \quad (\text{A8})$$

where $\hat{\mathcal{H}}_{\text{NL}}$ contains all nonquadratic terms and is given by

$$\hat{\mathcal{H}}_{\text{NL}} = g_0\hat{d}^\dagger\hat{d}(\hat{b} + \hat{b}^\dagger) - \frac{\mathcal{K}}{2}\hat{d}^{2\dagger}\hat{d}^2 - \mathcal{K}[\alpha^*\hat{d}^\dagger\hat{d}\hat{d} + \alpha\hat{d}^\dagger\hat{d}^\dagger\hat{d}]. \quad (\text{A9})$$

Here the first two terms are negligible, as they are not enhanced by the cavity field amplitude $|\alpha|$. Similarly, for sufficiently weak driving, the third term can also be neglected, as it is smaller by a factor of $|\alpha|$.

Furthermore, in the weak coupling regime $g_0 \ll \kappa$ we have that $g_0\langle\hat{x}\rangle/x_{\text{ZPF}}$ is small such that the effective cavity detuning can be denoted $\tilde{\Delta} = \Delta + 2\mathcal{K}|\alpha|^2$. Finally, the effective Hamiltonian obtained from the unitary transformation of Eq. (A1) is given by Eq. (4).

APPENDIX B: CAVITY BISTABILITY

We are interested in driving strengths that lead to a large average number of intracavity photons \bar{n}_c , but do not cause multistable solutions in the classical cavity dynamics. Following [46], the dynamics of the cavity average amplitude reads

$$\frac{d}{dt}\alpha = \left(i\Delta - \frac{\kappa}{2}\right)\alpha + i\mathcal{K}|\alpha|^2\alpha - i\sqrt{2}g_0\langle\hat{q}\rangle\alpha - \sqrt{\kappa}\alpha_{\text{in}}, \quad (\text{B1})$$

where $\hat{q} = (\hat{b} + \hat{b}^\dagger)/\sqrt{2}$ and α_{in} are the mechanical displacement quadrature operator and the coherent drive amplitude, respectively. Analogously, the classical dynamics of the mechanical mode are given by

$$\begin{aligned} \frac{d}{dt}\langle\hat{q}\rangle &= \omega_m\langle\hat{p}\rangle - \frac{\gamma_m}{2}\langle\hat{q}\rangle, \\ \frac{d}{dt}\langle\hat{p}\rangle &= -\omega_m\langle\hat{q}\rangle - \frac{\gamma_m}{2}\langle\hat{p}\rangle - \sqrt{2}g_0|\alpha|^2, \end{aligned} \quad (\text{B2})$$

with $\hat{p} = i(\hat{b}^\dagger - \hat{b})/\sqrt{2}$ and γ_m the momentum quadrature operator and the decay rate of the mechanical oscillator, respectively.

Since the oscillation of the mechanical position is small enough to weakly modulate the cavity field, we solve Eq. (B2) in the long time limit and find the steady state of the mechanical position operator

$$\langle\hat{q}\rangle_s = -\frac{\sqrt{2}g_0\omega_m|\alpha|^2}{\omega_m^2 + \frac{\gamma_m^2}{4}}, \quad (\text{B3})$$

which we insert into the equation for the classical cavity amplitude given in Eq. (B1) and obtain

$$\frac{d}{dt}\alpha = \left(i\Delta - \frac{\kappa}{2}\right)\alpha + i\mathcal{K}_{\text{eff}}\alpha|\alpha|^2 - \sqrt{\kappa}\alpha_{\text{in}}, \quad (\text{B4})$$

with the effective Kerr constant given in Eq. (6). The multiplication of the steady-state solution of Eq. (B4) with its complex conjugate yields ultimately the average photon occupation in Eq. (5). The possible values of the average cavity number can be explicitly calculated, yielding

$$|\alpha|_1^2 = \frac{1}{3\mathcal{K}_{\text{eff}}}\left(-2\Delta - \Sigma + \frac{\Lambda_0}{\Sigma}\right), \quad (\text{B5})$$

$$|\alpha|_{2,3}^2 = \frac{1}{3\mathcal{K}_{\text{eff}}}\left(-2\Delta + e^{\mp i\pi/3}\Sigma - e^{\pm i\pi/3}\frac{\Lambda_0}{\Sigma}\right), \quad (\text{B6})$$

where we introduced the definition $\Sigma = \sqrt[3]{\Lambda_0^3 + \Lambda_1^2 + \Lambda_1}$, with $\Lambda_0 = \frac{3\kappa^2}{4} - \Delta^2$ and $\Lambda_1 = -(\frac{9\kappa^2}{4} + \Delta^2)\Delta - \frac{27}{2}\kappa\mathcal{K}_{\text{eff}}\bar{n}_{\text{in}}$.

APPENDIX C: DERIVATION OF THE RADIATION PRESSURE FORCE SPECTRUM

The radiation pressure force spectrum describes the strength of the fluctuations of the cavity photon number at different frequencies. In the regime of linearized optomechanics this spectrum is obtained via

$$S_{FF}[\omega] = \int_{-\infty}^{\infty} d\omega' \langle \hat{F}[\omega] \hat{F}[\omega'] \rangle = g_0^2 S_{nn}[\omega], \quad (\text{C1})$$

where the linearized radiation pressure force is simply given by $\hat{F}[\omega] = G^*\hat{d}[\omega] + G\hat{d}^\dagger[\omega]$. For simplicity, here we rewrite the solution obtained in Eq. (11) as

$$\hat{d}[\omega] = -\frac{\sqrt{\kappa}}{\mathcal{N}[\omega]}(\mathcal{X}_c^{*-1}[-\omega]\hat{d}_{\text{in}} + i\Lambda\hat{d}_{\text{in}}^\dagger), \quad (\text{C2})$$

with the definition $\mathcal{N}[\omega] = \mathcal{X}_c^{*-1}[-\omega]\mathcal{X}_c^{-1}[\omega] - |\Lambda|^2$. This allows us to express the linearized radiation pressure force as

$$\hat{F}[\omega] = \eta^*[-\omega]\hat{d}_{\text{in}}[\omega] + \eta[\omega]\hat{d}_{\text{in}}^\dagger[\omega], \quad (\text{C3})$$

with

$$\eta[\omega] = -\frac{\sqrt{\kappa}}{\mathcal{N}[\omega]}(G\mathcal{X}_c^{-1}[\omega] + iG^*\Lambda). \quad (\text{C4})$$

Assuming δ -correlated noise as in Eq. (31), we find that the only nonzero contribution comes from the correlator $\langle\hat{d}_{\text{in}}[\omega']\hat{d}_{\text{in}}^\dagger[\omega]\rangle$ such that the spectrum of the radiation pressure force reads

$$S_{FF}[\omega] = \int \frac{d\omega'}{2\pi} \eta^*[-\omega]\eta[\omega']\langle\hat{d}_{\text{in}}[\omega]\hat{d}_{\text{in}}^\dagger[\omega']\rangle, \quad (\text{C5})$$

which coincides with Eq. (17) with the photon-number spectrum given by Eq. (13).

APPENDIX D: STOKES SUPPRESSION LIMITATION

In contrast to the work of Lau and Clerk [33], the two-mode optomechanical squeezing and Kerr-induced single-mode squeezing processes in our system are governed by a single phase ϕ_p , which originates from the cavity amplitude, as shown in Eq. (4). Consequently, it is not possible to independently tune these processes to cancel each other and suppress the heating mechanism. This limitation is evident in Eq. (17), where no real solution for $|\Lambda|$ exists that satisfies the condition $\Gamma_S = 0$.

APPENDIX E: DERIVATION OF THE AVERAGE MECHANICAL OCCUPATION

The occupation of the mechanical mode can be obtained using Eq. (25) with the noise spectrum given by Eq. (24), which can be calculated through the equation

$$S_{bb}[\omega] = \int \frac{d\Omega}{2\pi} \langle \hat{b}^\dagger[\Omega] \hat{b}[\omega] \rangle, \quad (\text{E1})$$

with $\hat{b}[\omega]$ given by Eq. (19), such that within the high- Q approximation Eq. (E1) becomes Eq. (24), whose poles \mathcal{P}_\pm become

$$\Omega_\pm = \pm(\mathcal{W}_R - i\mathcal{Z}_\pm), \quad (\text{E2})$$

where we define $\mathcal{W}_R - i\mathcal{W}_I \equiv \sqrt{\omega_m^2 - 2\omega_m\Sigma_c[\omega_m]}$ and $\mathcal{Z}_\pm \equiv \pm\gamma_m/2 + \mathcal{W}_I$.

To perform the integration of Eq. (24) via the residue theorem [58], we have to first perform a stability analysis of the poles. Here the only possible stable solution arises when $\mathcal{Z}_\pm > 0$. Moreover, under the assumption that $\Sigma_c[\omega_m]/\omega_m \ll 1$, we can make a Taylor expansion and find that $\mathcal{W}_R = \omega_m - \text{Re}(\Sigma_c[\omega_m])$ and $\mathcal{W}_I = \text{Im}(\Sigma_c[\omega_m])$. This is equivalent to neglecting the off-diagonal entries in the effective susceptibility matrix given by Eq. (22), which leads to

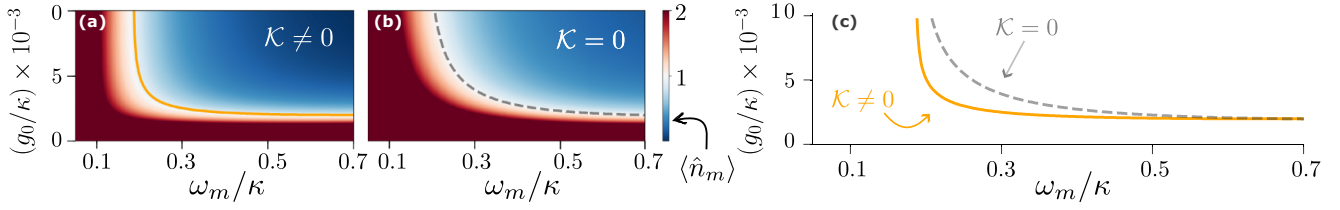


FIG. 12. Average phonon number as a function of the optomechanical coupling strength g_0/κ and resolved-sideband parameter ω_m/κ using (a) a nonlinear system and (b) a linear system. (c) The orange solid line and gray dashed line show the values for which the ground state is achieved in a nonlinear and a linear setup, respectively. Ground-state cooling can be obtained using a nonlinear cavity at both lower coupling strength and lower mechanical frequency as for an equivalent linear system. All other parameters are given in Table I.

off-resonant processes. Based on the previous analysis and using the residue theorem, we find the integrals

$$\begin{aligned} \int_{-\infty}^{\infty} \frac{d\omega}{2\pi} \frac{1}{|(\omega - \Omega_+)(\omega - \Omega_-)|^2} &\approx \frac{\mathcal{C}_{\text{eff}}}{2\omega_m^2 \gamma_m (\mathcal{C}_{\text{eff}}^2 - 1)}, \\ \int_{-\infty}^{\infty} \frac{d\omega}{2\pi} \frac{\omega}{|(\omega - \Omega_+)(\omega - \Omega_-)|^2} &\approx \frac{1}{2\omega_m \gamma_m (1 - \mathcal{C}_{\text{eff}}^2)}, \\ \int_{-\infty}^{\infty} \frac{d\omega}{2\pi} \frac{\omega^2}{|(\omega - \Omega_+)(\omega - \Omega_-)|^2} &\approx \frac{\mathcal{C}_{\text{eff}} [1 - (\frac{\gamma_m}{2\omega_m})^2]}{2\gamma_m (\mathcal{C}_{\text{eff}}^2 - 1)} \quad (\text{E3}) \end{aligned}$$

from which we obtain the average mechanical occupation given in Eq. (26).

APPENDIX F: MASTER-EQUATION APPROACH TO MECHANICAL OCCUPATION

If we work in the framework of an effective master equation for the mechanical mode we find that the average mechanical occupation follows Eq. (27) with the induced damping given by $\Gamma_{\text{opt}} = \Gamma_{\text{AS}} - \Gamma_{\text{S}}$ such that cooling is only possible if $\Gamma_{\text{AS}} > \Gamma_{\text{S}}$. The first term in Eq. (27) is effectively a modified mechanical thermal occupation, whereas the second term is what we know as the cavity backaction limit. Recalling that the cooperativity can be written in terms of the induced damping, since $\Gamma_{\text{opt}} = 2\text{Im}(\Sigma_c[\omega_m])$ and consequently $2\mathcal{C}_{\text{eff}} = \Gamma_{\text{opt}}/\gamma_m$, we find that Eq. (27) becomes

$$\bar{n}_m \approx \frac{\bar{n}_m^T}{1 + 2\mathcal{C}_{\text{eff}}} + \left(\frac{2\mathcal{C}_{\text{eff}}}{1 + 2\mathcal{C}_{\text{eff}}} \right) \frac{\Gamma_{\text{S}}}{\Gamma_{\text{opt}}}, \quad (\text{F1})$$

where the explicit substitution of the Stokes and anti-Stokes rates (17) results in Eq. (26).

APPENDIX G: MINIMAL OCCUPATION

We can combine our discussion in the main text and vary both parameters, the coupling strength and the resolved-sideband parameter, while keeping the input power at $\bar{n}_{\text{in}} = \bar{n}_{\text{in,crit}}$. In Fig. 12 we show when ground-state cooling is achieved as a function of the optomechanical coupling strength g_0/κ and the resolved-sideband parameter ω_m/κ . At

$g_0/\kappa = 0.85 \times 10^{-3}$, a nonlinear cavity (orange solid line) can cool to the ground state when $\omega_m/\kappa = 0.189$. Conversely, for the same input power, a linear system requires both a larger coupling strength of $g_0/\kappa = 1.79 \times 10^{-3}$ and a slightly larger mechanical frequency $\omega_m/\kappa = 0.192$. Hence, we find that the requirement for the resolved-sideband parameter to be at $\omega_m/\kappa > 0.177 \approx 0.2$ is a good approximation for ground-state cooling to be feasible and that it is necessary in both cases. However, for the same input power, the linear cavity requires roughly twice the coupling strength ratio g_0/κ . This again shows that a nonlinear cavity can cool at lower coupling strength in the unresolved-sideband regime.

APPENDIX H: SUPPRESSION OF THE STOKES PROCESS

In Sec. V we demonstrated that in the unresolved-sideband regime, a nonlinear cavity outperforms a linear system. Nevertheless, despite this improvement, cooling to the ground state in this regime is still constrained by the cavity backaction given explicitly in Eq. (28). Consequently, to overcome this limitation and cool below the backaction limit, we inject a squeezed vacuum, which can be externally generated by a degenerate parametric amplifier [45]. The dynamics of the DPA is described by the quantum Langevin equation

$$\dot{\hat{c}} = -\frac{\zeta}{2} \hat{c} + \chi \hat{c}^\dagger - \sqrt{\zeta} \hat{c}_{\text{in}}, \quad (\text{H1})$$

where $\sqrt{\zeta} \hat{c}_{\text{in}} = \sqrt{\zeta_{\text{S}}} \hat{c}_{\text{in,s}} + \sqrt{\zeta_{\text{v}}} \hat{c}_{\text{in,v}}$ is the input field, $\zeta = \zeta_{\text{S}} + \zeta_{\text{v}}$ is the total decay rate, and $\chi = |\chi| e^{-2i\varphi}$ is the squeezing parameter, with φ the squeezing angle. Here the input noise $\hat{c}_{\text{in,v}}$ corresponds to the intrinsic losses of the DPA, whose corresponding rate is given by ζ_{v} . On the other hand, $\hat{c}_{\text{in,s}}$ is related to the input-output port of the DPA, i.e., to the external modes of the electromagnetic field, which are controlled and used to drive the optomechanical system. The output field of the DPA is cascaded into the optomechanical system, yielding new cavity noise operators, which can be written as $\sqrt{\kappa} \hat{d}_{\text{in}} = \sqrt{\kappa_{\text{S}}} \hat{c}_{\text{out}} + \sqrt{\kappa_{\text{v}}} \hat{d}_{\text{in,v}}$, with $\kappa = \kappa_{\text{S}} + \kappa_{\text{v}}$ and $\hat{c}_{\text{out}} = \sqrt{\zeta_{\text{S}}} \hat{c} + \hat{c}_{\text{in,s}}$. Here \hat{c}_{out} is the output operator of the squeezed bath, which exchanges photons with the cavity at rate κ_{S} , and $\hat{d}_{\text{in,v}}$ is related to the uncontrolled losses of the cavity at rate κ_{v} . To quantify the combined intrinsic losses in the DPA and the nonlinear cavity, we define the loss parameter $\xi = \kappa_{\text{S}} \zeta_{\text{S}} / \kappa \zeta$. Using the white-noise approximation [59], the new noise correlators become Eq. (30) with the definitions Eq. (31). Similarly to Sec. IV, using the noise correlators in

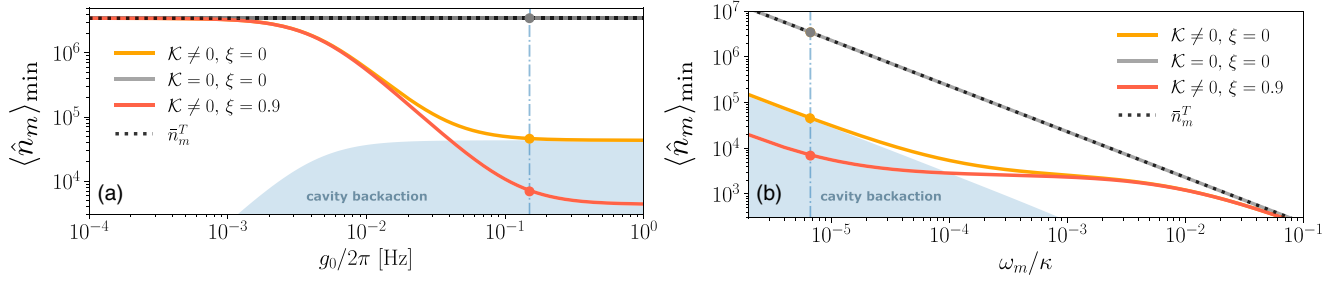


FIG. 13. Lowest phonon number as a function of (a) the optomechanical coupling strength and (b) the resolved-sideband parameter of a magnetically levitated mechanical system [60]. The gray solid line shows the cooling limit using a linear cavity, which coincides with the thermal occupation (black dotted line). The orange solid line corresponds to an equivalent nonlinear system, demonstrating suppression of thermal occupation by approximately 99% for the experimental parameters (vertical blue dash-dotted line). Additionally, the red solid line indicates the minimum phonon number achieved when a squeezed vacuum ($\xi = 0.9$) is injected into the nonlinear system, further improving the cooling limit beyond the cavity backaction limit (blue shaded area). The parameters used for this plot are $T = 20$ mK, $\omega_m/2\pi = 120$ Hz, $\kappa/2\pi = 18$ MHz, $\gamma_m/2\pi = 1.2$ μ Hz, $\mathcal{K}/2\pi = 1.4$ MHz, $g_0/2\pi = 0.15$ Hz, and $\bar{n}_{\text{in}} = \bar{n}_{\text{in, crit}}$.

Eq. (30), we derive the radiation pressure force spectrum

$$\begin{aligned} S_{FF}[\omega] &= S_{FF}^0[\omega] \left[1 + \left(1 + \frac{[\omega - \Delta_{\text{eff}}]^2 + \frac{\kappa^2}{4}}{[\omega + \Delta_{\text{eff}}]^2 + \frac{\kappa^2}{4}} \right) \xi N_s \right] \\ &\quad - \frac{2\xi M_s [(\Delta_{\text{eff}}^2 - \omega^2 - \frac{\kappa^2}{4}) \cos(2\varphi) - \Delta_{\text{eff}} \kappa \sin(2\varphi)]}{[\tilde{\Delta}^2 - \omega^2 + \frac{\kappa^2}{4} - |\Lambda|^2]^2 + \kappa^2 \omega^2}, \end{aligned} \quad (\text{H2})$$

which in the absence of squeezing, i.e., $\xi = 0$, we recover $S_{FF}^0[\omega] = g_0^2 S_{nn}^0[\omega]$ with the photon-number spectrum given by Eq. (13).

To minimize the Stokes process, an extrema analysis was conducted to determine the optimal squeezing phase, which is expressed as

$$\varphi = \frac{1}{2} \arctan \left(\frac{\kappa \Delta_{\text{eff}}}{\omega_m^2 - \Delta_{\text{eff}}^2 + \frac{\kappa^2}{4}} \right) + k\pi, \quad (\text{H3})$$

with $k \in \mathbb{Z}$. Hence, using the expression (H3), we find that the cavity backaction limit becomes Eq. (32) with \bar{n}_{BA} given by Eqs. (28) and (33). Note that in the absence of squeezing $\xi = 0$ in Eq. (32) we recover \bar{n}_{BA} , which is the backaction corresponding to a cavity with solely input vacuum noise. We can further minimize the backaction limit (32) over the properties of the squeezed input light and find that for $\varphi = \sqrt{N_s/(N_s + 1)}$ we obtain Eq. (34). As expected, in the absence of squeezing we recover Eq. (28), but for $\xi = 1$ we can fully suppress the quantum backaction limit.

In addition, we can quantify the amount of squeezing using the squeezing factor r , which is related to the noise correlators

in Eq. (31) through the relations

$$N_s = \frac{1}{\xi} \sinh^2(r), \quad M_s = \frac{1}{\xi} \sinh(r) \cosh(r). \quad (\text{H4})$$

Thus, from the condition yielding Eq. (34), we find that the squeezing factor is given by

$$\sinh^2(r) = \frac{\xi \delta^2}{1 - \delta^2} \geq 0, \quad (\text{H5})$$

with δ given by Eq. (33). Finally, in Fig. 10 we measured the squeezing in units of decibels using the formula

$$\varrho = -10 \log_{10}(e^{-2r}). \quad (\text{H6})$$

APPENDIX I: MAGNETICALLY LEVITATED SYSTEMS

Various platforms currently explore the inductive coupling of center-of-mass mechanical motion with superconducting resonators. These mechanical systems can be broadly classified into levitated [60] and clamped [40] configurations, with resonance frequencies on the order of 100 Hz and megahertz, respectively. This broad frequency range allows access to distinct parameter regimes, including variations in mass and spatial superposition size, thereby enabling the ability of quantum state control. However, in both cases, the generation of nonclassical states is significantly limited by the high thermal occupation of these systems. Consequently, the development of advanced cooling techniques is crucial for achieving ground-state cooling in such mechanical platforms. In this regard, the nonlinear cavity significantly improves cooling performance even within the parameter regime of levitated systems, surpassing the limits of a linear setup for the same driving power, as demonstrated in Fig. 13.

- [1] B. C. Barish and R. Weiss, *Phys. Today* **52** (10), 44 (1999).
- [2] C. M. Caves, K. S. Thorne, R. W. P. Drever, V. D. Sandberg, and M. Zimmermann, *Rev. Mod. Phys.* **52**, 341 (1980).

- [3] M. Aspelmeyer, T. J. Kippenberg, and F. Marquardt, *Rev. Mod. Phys.* **86**, 1391 (2014).
- [4] J. D. Teufel, T. Donner, M. A. Castellanos-Beltran, J. W. Harlow, and K. W. Lehnert, *Nat. Nanotechnol.* **4**, 820 (2009).

- [5] D. Mason, J. Chen, M. Rossi, Y. Tsaturyan, and A. Schliesser, *Nat. Phys.* **15**, 745 (2019).
- [6] E. E. Wollman, C. U. Lei, A. J. Weinstein, J. Suh, A. Kronwald, F. Marquardt, A. A. Clerk, and K. C. Schwab, *Science* **349**, 952 (2015).
- [7] A. Zivari, R. Stockill, N. Fiaschi, and S. Gröblacher, *Nat. Phys.* **18**, 789 (2022).
- [8] J. D. Teufel, D. Li, M. S. Allman, K. Cicak, A. J. Sirois, J. D. Whittaker, and R. W. Simmonds, *Nature (London)* **471**, 204 (2011).
- [9] A. de los Ríos Sommer, N. Meyer, and R. Quidant, *Nat. Commun.* **12**, 276 (2021).
- [10] S. Barzanjeh, A. Xuereb, S. Gröblacher, M. Paternostro, C. A. Regal, and E. M. Weig, *Nat. Phys.* **18**, 15 (2022).
- [11] C.-H. Bai, D.-Y. Wang, H.-F. Wang, A.-D. Zhu, and S. Zhang, *Sci. Rep.* **7**, 2545 (2017).
- [12] F. Marquardt, A. A. Clerk, and S. M. Girvin, *J. Mod. Opt.* **55**, 3329 (2008).
- [13] M. Rossi, D. Mason, J. Chen, Y. Tsaturyan, and A. Schliesser, *Nature (London)* **563**, 53 (2018).
- [14] F. Tebbenjohanns, M. Frimmer, V. Jain, D. Windey, and L. Novotny, *Phys. Rev. Lett.* **124**, 013603 (2020).
- [15] J. D. Teufel, T. Donner, D. Li, J. W. Harlow, M. S. Allman, K. Cicak, A. J. Sirois, J. D. Whittaker, K. W. Lehnert, and R. W. Simmonds, *Nature (London)* **475**, 359 (2011).
- [16] J. Chan, T. P. M. Alegre, A. H. Safavi-Naeini, J. T. Hill, A. Krause, S. Gröblacher, M. Aspelmeyer, and O. Painter, *Nature (London)* **478**, 89 (2011).
- [17] S. Mancini, D. Vitali, and P. Tombesi, *Phys. Rev. Lett.* **80**, 688 (1998).
- [18] C. Genes, D. Vitali, P. Tombesi, S. Gigan, and M. Aspelmeyer, *Phys. Rev. A* **77**, 033804 (2008).
- [19] F. Marquardt and S. M. Girvin, *Physics* **2**, 40 (2009).
- [20] J. Guo and S. Gröblacher, *Quantum* **6**, 848 (2022).
- [21] M. Ernzer, M. Bosch Aguilera, M. Brunelli, G.-L. Schmid, T. M. Karg, C. Bruder, P. P. Potts, and P. Treutlein, *Phys. Rev. X* **13**, 021023 (2023).
- [22] J.-Y. Yang, D.-Y. Wang, C.-H. Bai, S.-Y. Guan, X.-Y. Gao, A.-D. Zhu, and H.-F. Wang, *Opt. Express* **27**, 22855 (2019).
- [23] Y.-C. Liu, Y.-F. Xiao, X. Luan, Q. Gong, and C. W. Wong, *Phys. Rev. A* **91**, 033818 (2015).
- [24] D.-Y. Wang, C.-H. Bai, S. Liu, S. Zhang, and H.-F. Wang, *Phys. Rev. A* **98**, 023816 (2018).
- [25] F. Elste, S. M. Girvin, and A. A. Clerk, *Phys. Rev. Lett.* **102**, 207209 (2009).
- [26] N. Carlon Zambon, Z. Denis, R. De Oliveira, S. Ravets, C. Ciuti, I. Favero, and J. Bloch, *Phys. Rev. Lett.* **129**, 093603 (2022).
- [27] C. Genes, H. Ritsch, and D. Vitali, *Phys. Rev. A* **80**, 061803(R) (2009).
- [28] M. Asjad, S. Zippilli, and D. Vitali, *Phys. Rev. A* **94**, 051801(R) (2016).
- [29] J. B. Clark, F. Lecocq, R. W. Simmonds, J. Aumentado, and J. D. Teufel, *Nature (London)* **541**, 191 (2017).
- [30] S. Huang and G. S. Agarwal, *Phys. Rev. A* **79**, 013821 (2009).
- [31] J.-H. Gan, Y.-C. Liu, C. Lu, X. Wang, M. K. Tey, and L. You, *Laser Photonics Rev.* **13**, 1900120 (2019).
- [32] B. Xiong, X. Li, S.-L. Chao, Z. Yang, R. Peng, and L. Zhou, *Ann. Phys. (Berlin)* **532**, 1900596 (2020).
- [33] H.-K. Lau and A. A. Clerk, *Phys. Rev. Lett.* **124**, 103602 (2020).
- [34] M. Asjad, N. E. Abari, S. Zippilli, and D. Vitali, *Opt. Express* **27**, 32427 (2019).
- [35] P. D. Nation, M. P. Blencowe, and E. Buks, *Phys. Rev. B* **78**, 104516 (2008).
- [36] C. Laflamme and A. A. Clerk, *Phys. Rev. A* **83**, 033803 (2011).
- [37] D. Zoepfl, M. L. Juan, N. Diaz-Naufal, C. M. F. Schneider, L. F. Deeg, A. Sharafiev, A. Metelmann, and G. Kirchmair, *Phys. Rev. Lett.* **130**, 033601 (2023).
- [38] I. C. Rodrigues, D. Bothner, and G. A. Steele, *Nat. Commun.* **10**, 5359 (2019).
- [39] D. Zoepfl, M. L. Juan, C. M. F. Schneider, and G. Kirchmair, *Phys. Rev. Lett.* **125**, 023601 (2020).
- [40] P. Schmidt, M. T. Amawi, S. Pogorzalek, F. Deppe, A. Marx, R. Gross, and H. Huebl, *Commun. Phys.* **3**, 233 (2020).
- [41] T. Luschmann, P. Schmidt, F. Deppe, A. Marx, A. Sanchez, R. Gross, and H. Huebl, *Sci. Rep.* **12**, 1608 (2022).
- [42] D. Bothner, I. C. Rodrigues, and G. A. Steele, *Commun. Phys.* **5**, 33 (2022).
- [43] T. Bera, M. Kandpal, G. S. Agarwal, and V. Singh, *Nat. Commun.* **15**, 7115 (2024).
- [44] O. Shevchuk, G. A. Steele, and Y. M. Blanter, *Phys. Rev. B* **96**, 014508 (2017).
- [45] H. J. Carmichael, G. J. Milburn, and D. F. Walls, *J. Phys. A: Math. Gen.* **17**, 469 (1984).
- [46] C. W. Gardiner and M. J. Collett, *Phys. Rev. A* **31**, 3761 (1985).
- [47] S. Aldana, C. Bruder, and A. Nunnenkamp, *Phys. Rev. A* **88**, 043826 (2013).
- [48] A. Dorsel, J. D. McCullen, P. Meystre, E. Vignes, and H. Walther, *Phys. Rev. Lett.* **51**, 1550 (1983).
- [49] M. Müller and I. Rotter, *J. Phys. A: Math. Theor.* **41**, 244018 (2008).
- [50] A. A. Clerk, M. H. Devoret, S. M. Girvin, F. Marquardt, and R. J. Schoelkopf, *Rev. Mod. Phys.* **82**, 1155 (2010).
- [51] L. F. Deeg, D. Zoepfl, N. Diaz-Naufal, M. L. Juan, A. Metelmann, and G. Kirchmair, *Phys. Rev. Appl.* **23**, 014082 (2025).
- [52] T. Ojanen and K. Børkje, *Phys. Rev. A* **90**, 013824 (2014).
- [53] Y.-C. Liu, Y.-F. Xiao, X. Luan, and C. W. Wong, *Phys. Rev. Lett.* **110**, 153606 (2013).
- [54] J. B. Clark, F. Lecocq, R. W. Simmonds, J. Aumentado, and J. D. Teufel, *Nat. Phys.* **12**, 683 (2016).
- [55] J. Monsel, N. Dashti, S. K. Manjeshwar, J. Eriksson, H. Ernbrink, E. Olsson, E. Torneus, W. Wiecek, and J. Splettstoesser, *Phys. Rev. A* **103**, 063519 (2021).
- [56] U. L. Andersen, T. Gehring, C. Marquardt, and G. Leuchs, *Phys. Scr.* **91**, 053001 (2016).
- [57] J. Sakurai and J. Napolitano, *Modern Quantum Mechanics* (Cambridge University Press, Cambridge, 2017).
- [58] S. Lang, *Complex Analysis* (Springer, New York, 1999).
- [59] C. Gardiner and P. Zoller, *Quantum Noise* (Springer, Berlin, 2004).
- [60] M. Gutierrez Latorre, G. Higgins, A. Paradkar, T. Bauch, and W. Wiecek, *Phys. Rev. Appl.* **19**, 054047 (2023).